Article

Neuron

Multiple Running Speed Signals in Medial Entorhinal Cortex

Highlights

- Two dissociable running speed signals are present in medial entorhinal cortex (MEC)
- Medial septal inactivation strengthens the firing rate speed signal in MEC
- Speed modulation of intrinsic theta frequency is decreased during MS inactivation
- A sizable percentage of MEC neurons are negatively speed modulated

Authors

James R. Hinman, Mark P. Brandon, Jason R. Climer, G. William Chapman, Michael E. Hasselmo

Correspondence

hinman@bu.edu

In Brief

Hinman et al. demonstrate the presence of multiple running speed signals in medial entorhinal cortex that are differentially dependent upon intact medial septal input. Running speed signals are a critical component in models of grid cell generation.

Hinman et al., 2016, Neuron *91*, 666–679
August 3, 2016
http://dx.doi.org/10.1016/j.neuron.2016.06.027

CellPress

CellPress

Neuron
Article

Multiple Running Speed Signals in Medial Entorhinal Cortex

James R. Hinman,[1,*] Mark P. Brandon,[1,3] Jason R. Climer,[1,2] G. William Chapman,[1] and Michael E. Hasselmo[1,2]
[1]Department of Psychological and Brain Sciences, Center for Systems Neuroscience, Center for Memory and Brain
[2]Graduate Program for Neuroscience
Boston University, 2 Cummington Mall, Boston, MA 02215, USA
[3]Present address: Department of Psychiatry, Douglas Mental Health University Institute, McGill University, Montreal, QC H4H 1R3, Canada
*Correspondence: hinman@bu.edu
http://dx.doi.org/10.1016/j.neuron.2016.06.027

SUMMARY

Grid cells in medial entorhinal cortex (MEC) can be modeled using oscillatory interference or attractor dynamic mechanisms that perform path integration, a computation requiring information about running direction and speed. The two classes of computational models often use either an oscillatory frequency or a firing rate that increases as a function of running speed. Yet it is currently not known whether these are two manifestations of the same speed signal or dissociable signals with potentially different anatomical substrates. We examined coding of running speed in MEC and identified these two speed signals to be independent of each other within individual neurons. The medial septum (MS) is strongly linked to locomotor behavior, and removal of MS input resulted in strengthening of the firing rate speed signal, while decreasing the strength of the oscillatory speed signal. Thus, two speed signals are present in MEC that are differentially affected by disrupted MS input.

INTRODUCTION

The medial entorhinal cortex (MEC) is a critical component of the brain's spatial navigation system. Grid cells in MEC are spatially modulated neurons with firing fields on the vertices of tessellating triangles covering the entire environment (Fyhn et al., 2004; Hafting et al., 2005). The regular nature of grid cell spatial receptive fields has led to the suggestion that they are path integrators (McNaughton et al., 2006), neurons that track relative location within an environment based on the speed and direction of an animal's movement. Two general classes of computational models have been employed to generate the spatially repeating firing pattern of grid cells using either oscillatory interference or attractor dynamics (McNaughton et al., 2006; Fuhs and Touretzky, 2006; Guanella and Verschure, 2006; Burgess et al., 2007; Burgess, 2008; Hasselmo, 2008; Blair et al., 2008; Burak and Fiete, 2009; Navratilova et al., 2012; for review, see Zilli 2012), although recent models have combined elements of both of these approaches (Hasselmo and Brandon, 2012; Schmidt-Hieber and Häusser, 2013; Hasselmo and Shay, 2014; Bush and Burgess, 2014). All of these models require a running speed signal to code for movement through space, although the mechanisms employed to generate grid cell firing differ in a number of key respects across models. The speed signal is generally modeled with oscillatory activity that varies in frequency as a function of running speed or a firing rate that varies linearly as a function of running speed in oscillatory interference and attractor dynamics models, respectively. Recent modeling work from our lab has also suggested that MEC interneurons with either speed modulation of intrinsic oscillatory frequency or firing rates may be responsible for speed coding in MEC and thus be critical for the generation of grid cells (Hasselmo and Shay, 2014).

The two signals necessary for path integration computations have been experimentally demonstrated to be present in MEC. Neurons coding for head direction (HD) arise in an ascending circuit, beginning in the lateral mammillary nucleus that ultimately reaches MEC (Taube, 2007; Sargolini et al., 2006). The disruption of HD input to MEC disrupts grid cell spatial periodicity, as predicted by computational models (Winter et al., 2015). Speed-modulated activity is present in a diverse set of brain regions, including MEC (Sargolini et al., 2006; Jeewajee et al., 2008; Wills et al., 2012), with a recent report demonstrating a dedicated group of speed cells in MEC cells that code running speed through their firing rates (Kropff et al., 2015). Speed signals have been shown in MEC principal neurons as increases in firing rates as a function of running speed (Sargolini et al., 2006; Wills et al., 2012; Kropff et al., 2015), and similarly in MEC interneurons (Buetfering et al., 2014; Kropff et al., 2015). In addition, the intrinsic theta frequency oscillatory firing of MEC grid cells is positively modulated by running speed (Jeewajee et al., 2008), while similar information is not currently available for MEC interneurons. It is currently not known whether the increases in firing rate and theta oscillatory frequency as a function of running speed are different physiological manifestations of the same speed signal impinging upon MEC circuits or dissociable signals with potentially different anatomical substrates. In fact, to date the anatomical pathways by which running speed information reaches MEC circuits have yet to be elucidated.

The medial septum (MS) is well positioned anatomically to influence the ongoing activity of neurons throughout the entorhinal

cortex since it projects across the entire dorso-ventral axis (Alonso and Köhler, 1984). Theta oscillations in the local field potential (LFP) throughout the hippocampal formation, which are dependent upon the MS (Winson, 1978; Mitchell et al., 1982; Mizumori et al., 1990; Buzsáki, 2002), have long been linked to locomotor behavior (Vanderwolf, 1969). The frequency of theta oscillations throughout the entorhinal cortex and hippocampus is positively modulated by running speed (Rivas et al., 1996; Sławińska and Kasicki, 1998; Jeewajee et al., 2008; Hinman et al., 2011). Several classes of theta phase-locked interneurons in the hippocampus have speed-modulated firing rates, while several additional classes of hippocampal interneurons that are not theta phase locked lack speed-modulated firing rates (Czurkó et al., 2011). Within the MS itself, neurons have firing rates that vary as a function of running speed (Zhou et al., 1999), and the theta rhythmic burst frequency of MS neurons is modulated by running speed (King et al., 1998; Zhou et al., 1999; Welday et al., 2011), with a subpopulation of these cells also exhibiting head directional tuning (King et al., 1998; Zhou et al., 1999). Additionally, glutamatergic neurons in MS are strongly linked to locomotor behavior, as optogenetic stimulation has been shown to induce running behavior and to be responsible for the running speed modulation of the firing rates of neurons in the hippocampus (Fuhrmann et al., 2015). Thus, both anatomical and physiological data point to MS as a potential substrate by which the speed signal necessary for normal grid cell firing reaches MEC.

RESULTS

Linear and Saturating Increases in Firing Rate

Running speed information is critical to models of grid cell generation, which generally employ a positive linear running speed signal. Thus, we first sought to identify the nature by which the firing rates of MEC neurons respond as a function of running speed. A total of 332 cells were recorded from MEC as rats foraged in an open-field environment, which included grid cells (n = 45), conjunctive grid-by-head direction cells (n = 20), HD cells (n = 157), border cells (n = 14), spatially uncharacterized cells (n = 65), and interneurons (n = 31). Many MEC neurons' firing rates increase as a function of running speed (Sargolini et al., 2006; Wills et al., 2012; Kropff et al., 2015), and this increase appeared linear in response to running speed in numerous neurons, although many neurons appeared to have firing rates that plateaued after the animal reached moderate speeds and thus were not fit well with a linear function. Therefore, we employed a maximum likelihood estimation approach to parametrically optimize the fit between running speed and firing rate to both a linear and saturating exponential curve for each cell separately. For both fits, we conducted an F test comparing each fit to a uniform fit with the p value threshold for the F tests set based on a spike shuffling procedure such that greater than 99% of a shuffled p value distribution lay above those of the cells we identified as significantly speed modulated. Next, we performed a nested model comparison between the two fits, using an F test with a linear fit as the null hypothesis. This required the saturating exponential model to reduce the error of the fit enough to justify the additional terms of the saturating exponential function. The result of this approach was the determination for each cell of whether (1) its firing rate was statistically significantly modulated by running speed and (2) it was significantly better fit with a saturating exponential function than a linear function (Figures 1A and 1B). This approach was applied using a point estimate on spikes temporally binned to individual video frames (~33 ms) of all behavioral epochs with a running speed greater than 2 cm s^{-1} in order to ensure that we did not incorrectly identify firing rate changes due to behavioral state as changes due to running speed.

Overall, ~78% of MEC neurons had firing rates that were significantly modulated by running speed (260 out of 332 total MEC cells), with the majority of each cell type showing statistically significant modulation of firing rate by running speed (Figure 1C; grid, 31/45; conjunctive, 16/20; HD, 127/157; uncharacterized, 47/65; interneuron, 28/31). We identified similar proportions of speed-modulated neurons through the use of multiple different approaches, including by binning the data based on running speed (~70%), as has been previously reported (McNaughton et al., 1983; Wills et al., 2012; Figure S1A, available online), as well as through the use of only linear regression on temporal bins and a shuffling procedure for the determination of significant speed modulation (~65% with r values < 1st percentile or >99th percentile; Kropff et al., 2015; Figures S1B and S1E). The use of speed bins appears to overestimate the strength of the relationship between firing rate and running speed (Figures S1D–S1F), likely due to averaging out variability in the firing rate dependent on other factors, but the best-fit functions obtained using temporal and speed bins were very similar. Both the slopes and y-intercepts estimated by the two methods were highly correlated (slope, $r = 0.87$, $p < 1 \times 10^{-10}$; y-intercept, $r = 0.98$, $p < 1 \times 10^{-10}$; Figures S1G and S1H), although the use of temporal bins resulted in slightly lower slopes (Wilcoxon signed-rank test; $p < 5 \times 10^{-8}$) and slightly higher y-intercepts (Wilcoxon signed-rank test; $p < 1 \times 10^{-10}$) than those obtained through the use of speed bins. The correspondence between the two approaches can be seen in each plot of firing rate versus running speed throughout the paper (Figures 1A, 1B, 2E, 3A–3D, 5B, 6B, and 6C), which show the best-fit line and confidence intervals based on temporal binning (light red or light blue) overlaid on the estimated firing rate and confidence intervals based on binning the data using running speed bins (black dots and gray shading).

The path integration mechanisms employed in grid cell models require the running speed signal to be linear in nature, which previous accounts of speed modulation have generally assumed rather than explicitly tested. Of the 260 cells identified as having significant speed modulation of their firing rate, the majority were actually better fit using a saturating exponential (which we refer to as "saturating cells") function rather than a linear function (Figure 1C; 145 of 260). Similar proportions of saturating and linear cells were identified for each putative principal cell type (Figure 1C; grid, 36% saturating/33% linear; conjunctive, 35% saturating/45% linear; HD, 44% saturating/37% linear; uncharacterized, 37% saturated/35% linear). For interneurons, an overwhelming majority were better fit with the saturating exponential function rather than the linear function (Figure 1C; interneuron, 77% saturating/13% linear). Overall,

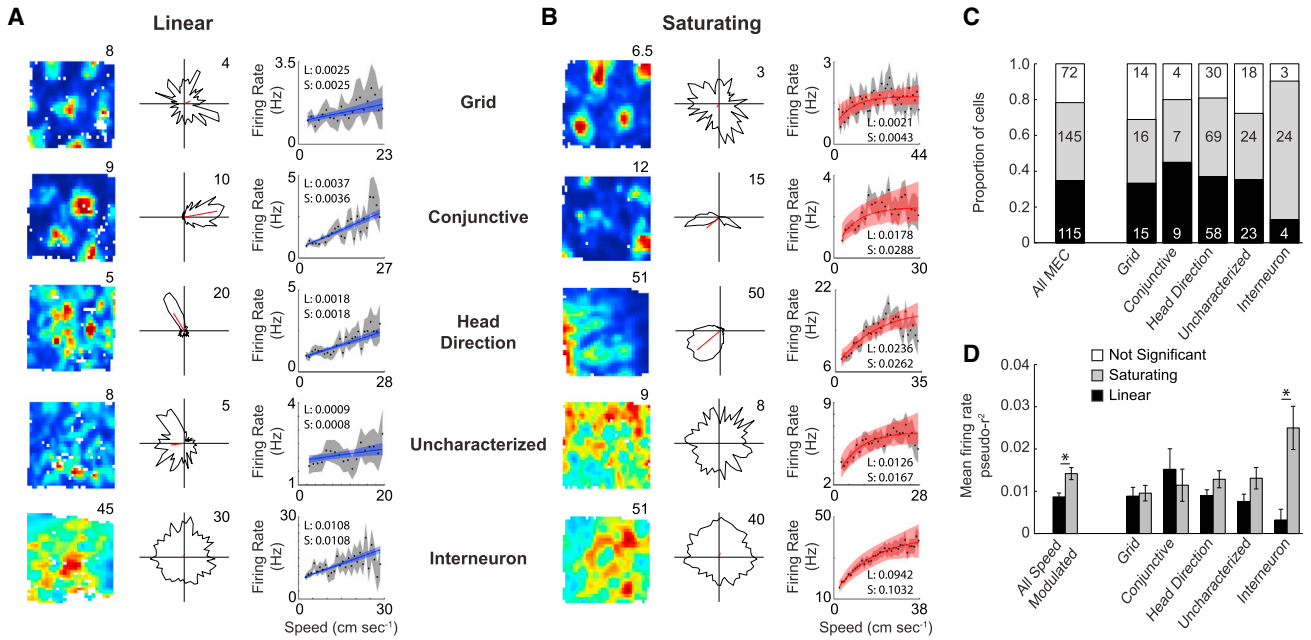

Figure 1. Linear and Saturating Coding of Running Speed by the Firing Rate of MEC Neurons

(A) Spatial rate map (left), HD polar plot (middle), and firing rate versus running speed plot (right) for a grid cell, conjunctive cell, HD cell, uncharacterized cell, and interneuron (top to bottom) that linearly code running speed. Each plot shows the best-fit function with confidence intervals (blue and red for linear and saturating cells, respectively), as obtained using maximum likelihood estimation on temporal bins, and also shows the mean value of running speed bins (black dots) and associated confidence intervals (gray). The inset values in each plot are the pseudo-r^2 values for the linear (L) and saturating (S) fits.

(B) Same as in (A), but for saturating cells.

(C) Proportions of each cell type coding running speed linearly and exponentially. The values indicate the number of cells.

(D) Mean ± SEM firing rate pseudo-r^2 values for linear and saturating cells. *p < 0.005.

saturating cells had higher firing rate pseudo-r^2 values than linear cells (Figure 1D; Wilcoxon rank-sum test, $p < 0.005$), although this appeared to be primarily mediated by interneurons, as they were the only cell type to show a difference between the firing rate pseudo-r^2 values for saturating and linear cells (Figure 1D; Wilcoxon rank-sum test, $p < 0.01$). Thus, the vast majority of neurons in MEC have speed-modulated firing rates, but the firing rates of most speed-modulated neurons saturate and therefore do not linearly follow running speed across the full range of behaviorally manifested running speeds, and this did not result from the animal reaching higher maximum speeds during sessions where saturating cells were identified (Wilcoxon rank-sum test, not significant [n.s.]; Figures S1I and S1J).

Having statistically identified speed-modulated neurons, whether linear or saturating, we next sought to confirm the positive nature of the relationship between firing rate and running speed, as has been previously observed (Sargolini et al., 2006). We calculated the speed modulation of each significantly speed-modulated cell as the difference between the firing rate predicted by the best-fit line (either linear or saturating) at the maximum and minimum running speed divided by the difference in maximum and minimum running speed. Overall, the speed modulation of firing rates of MEC neurons was positive (Figure 2A; Wilcoxon signed-rank test, $p < 1 \times 10^{-10}$), which was the case for each individual cell type as well (Figure 2A; Wilcoxon signed-rank test; grid, $p < 1 \times 10^{-6}$; conjunctive, $p < 0.0005$; HD, $p < 1 \times 10^{-9}$; uncharacterized, $p < 1 \times 10^{-7}$; interneuron, $p < 1 \times 10^{-5}$). The median predicted firing rate when the animal's speed goes to zero (y-intercept) was also positive for the speed-modulated MEC cells (Figure 2B; Wilcoxon signed-rank test, $p < 1 \times 10^{-10}$), as well as for each individual cell type (Figure 2B; Wilcoxon signed-rank test; grid, $p < 1 \times 10^{-6}$; conjunctive, $p < 0.0005$; HD, $p < 1 \times 10^{-10}$; uncharacterized, $p < 0.001$; interneuron, $p < 1 \times 10^{-5}$). The interneurons appeared to have greater variability of their slopes and y-intercepts, which may be due to the fact that there is a great deal of heterogeneity in mean firing rate among molecularly distinct interneurons that cannot be differentiated based on extracellular recordings.

Despite the average positive nature of the speed modulation of MEC cells, a sizable proportion actually show negative speed modulation (Figures 2C–2E; 42/260 = 16%). This facet of speed modulation in MEC is especially apparent when considering the r values for the relationship between firing rate and running speed, as cells can be seen to fall on either side of zero (Figure 2C). The majority of cells have a strong, positive relationship between firing rate and running speed, yet the negatively speed-modulated cells also appear to have a strong relationship between firing rate and running speed, albeit in the opposite direction. The positively speed-modulated cells have a slightly stronger relationship between firing rate and running speed than the

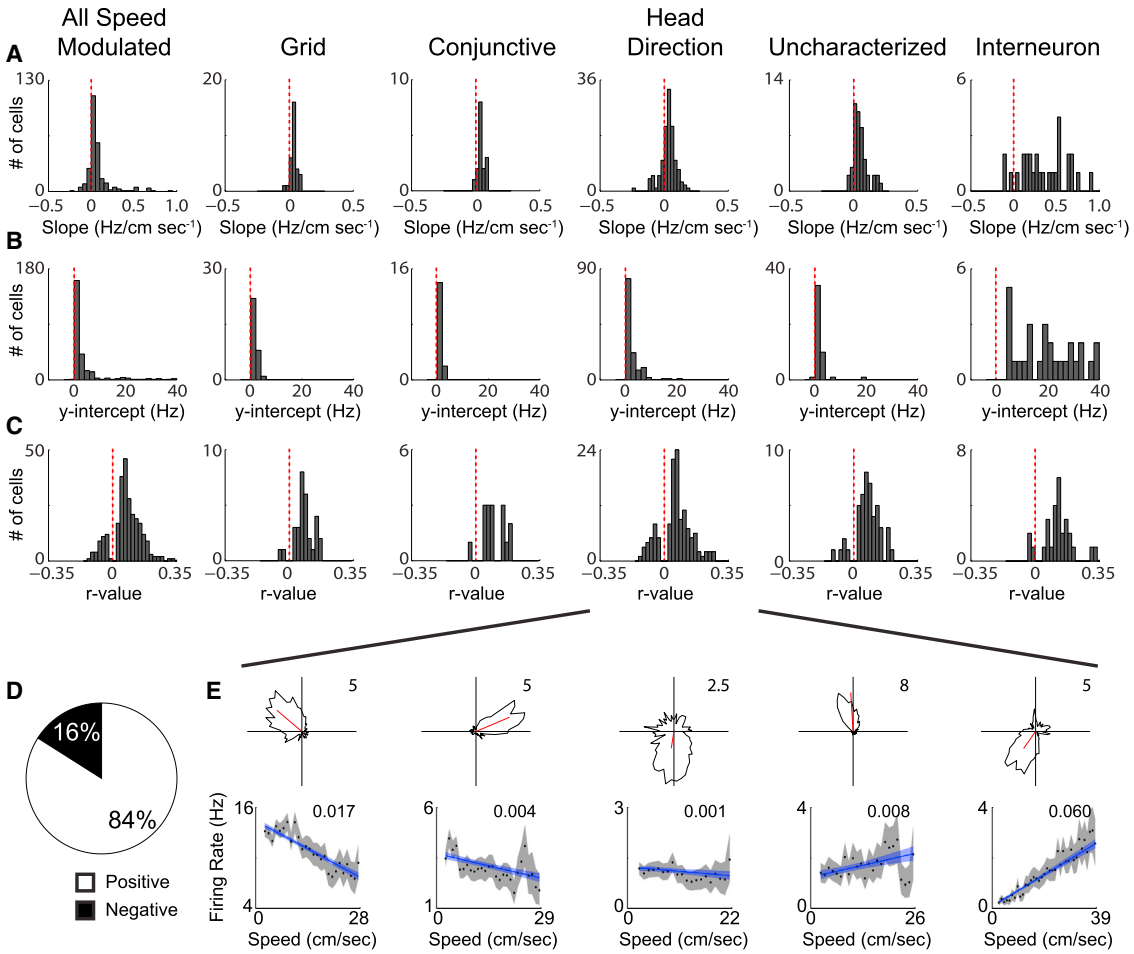

Figure 2. A Subset of Negatively Speed-Modulated MEC Cells

(A) Distributions of the slope between firing rate and running speed.

(B) Distributions of y-intercepts of relationship between firing rate and running speed.

(C) Distributions of r values between firing rate and running speed.

(D) Proportion of positively and negatively speed-modulated cells.

(E) HD polar plots (top) and firing rate versus running speed plots (bottom) for five HD cells with significant firing rate speed modulation, but with varying magnitudes and polarities of speed modulation. The inset value in each plot is the firing rate pseudo-r^2 value for the linear fit.

negatively modulated cells (positive cells, median pseudo r^2 = 0.007; negative cells, median pseudo-r^2 = 0.003; Wilcoxon rank-sum test, $p < 1 \times 10^{-6}$). The majority of negatively modulated cells were HD cells (26 out of 42 negatively modulated cells), although negative speed modulation was not restricted to HD cells, and there was no apparent relationship between the strength of head directional tuning and the direction or degree of speed modulation (Figure 2E). Cells carrying this negative firing rate speed signal were recorded simultaneously on the same tetrode with cells carrying the positive firing rate speed signal, so both speed signals are present in highly localized areas within MEC.

Increased Theta Oscillatory Frequency as a Function of Running Speed

In addition to the firing rate of MEC neurons being modulated by running speed, the amplitude and frequency of theta rhythmicity throughout the hippocampal formation is also positively modulated by running speed both in the LFP (McFarland et al., 1975; Sławińska and Kasicki, 1998; Hinman et al., 2011) and the spiking of individual neurons (Jeewajee et al., 2008; Maurer et al., 2005; Welday et al., 2011; Stensola et al., 2012; Figures 3A–3D). Recent simulations of the generation of grid cells either assume or generate interneuron firing properties with speed-modulated theta frequency spiking that induces rebound spiking in grid cells (Hasselmo and Shay, 2014; Hasselmo, 2013). Here we employed a recently developed technique utilizing maximum likelihood estimation to determine attributes of theta rhythmic firing (Climer et al., 2015), such as modulation depth and intrinsic frequency, and we conditionalized these features of rhythmicity on running speed. This provides information regarding the manner in which theta rhythmic firing varies as a function of running speed. Overall, the majority of MEC cells exhibited significant theta rhythmic spiking irrespective of speed (all MEC,

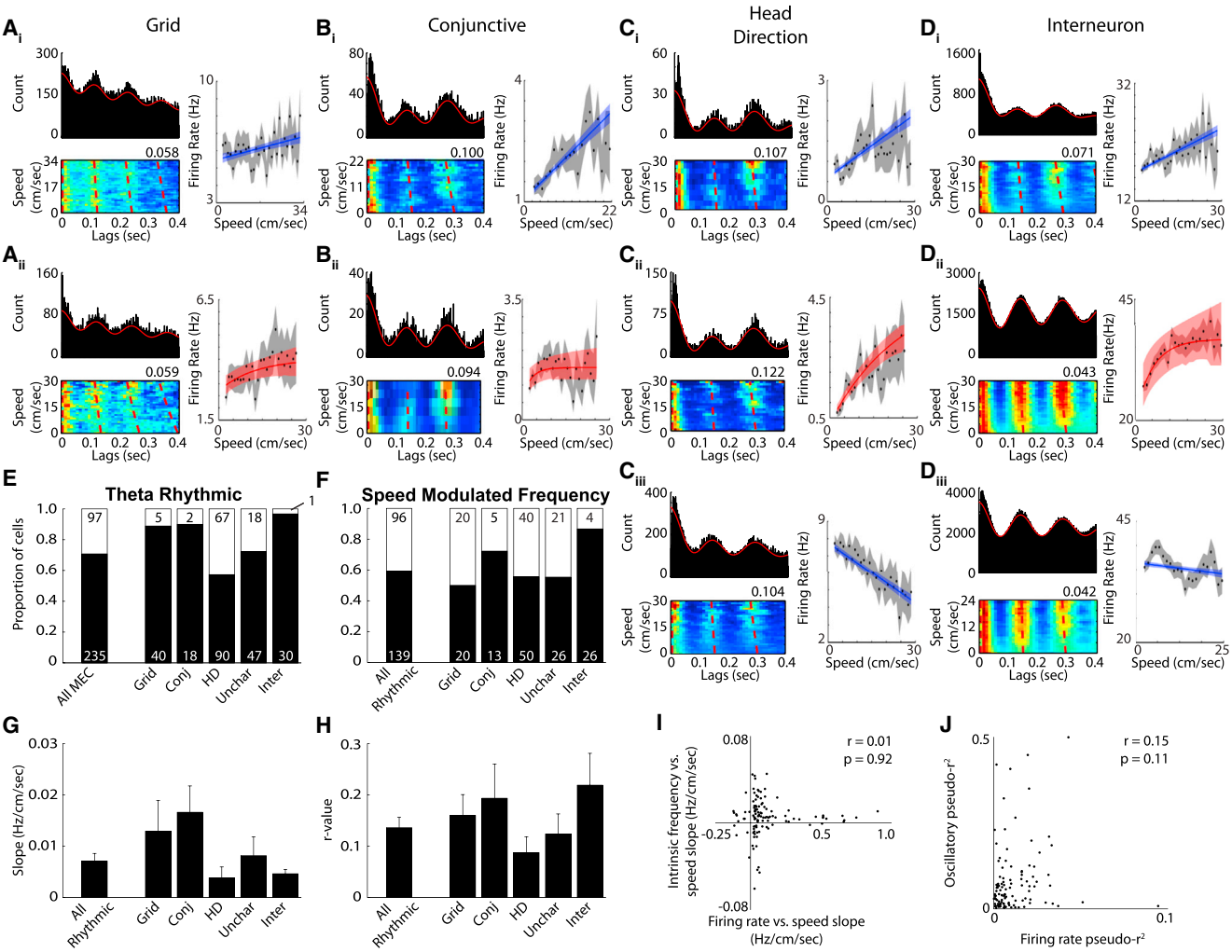

Figure 3. Speed Modulation of Oscillatory Theta Frequency

(A–D) Three plots are shown each for example grid cells (A), conjunctive cells (B), HD cells (C), and interneurons (D). Traditional autocorrelations showing theta rhythmicity (top left plot), spike time lags as a function of running speed (the value at the top right corner of each plot indicates the maximum conditional probability of firing [red] shown in the plot with the sum of each running speed row equaling a conditional probability of 1) (bottom left plot), and firing rate versus running speed (right).

(A_i–D_i) Grid cells (A_i), conjunctive cells (B_i), HD cells (C_i), and interneurons (D_i) with positive linear relationships between firing rate and running speed.

(A_{ii}–D_{ii}) Grid cells (A_{ii}), conjunctive cells (B_{ii}), HD cells (C_{ii}), and interneurons (D_{ii}) with saturating relationships between firing rate and running speed.

(C_{iii} and D_{iii}) HD cells (C_{iii}) and interneurons (D_{iii}) with negative linear relationships between firing rate and running speed.

(E) The proportion of cells with significant theta modulation.

(F) The proportion of theta rhythmic neurons with significantly speed-modulated oscillatory frequencies.

(G) The mean ± SEM slope of the relationship between oscillatory frequency and running speed.

(H) The mean ± SEM r value of the relationship between oscillatory frequency and running speed.

(I) There is no relationship between the firing rate versus running speed slopes and the oscillatory frequency versus running speed slopes.

(J) There is no relationship between the firing rate pseudo-r^2 values and the oscillatory frequency pseudo-r^2 values.

235/322; Figure 3E), with 65 out of the 235 theta rhythmic cells displaying theta cycle skipping (Brandon et al., 2013), and this was the case for each individual cell type as well (grid, 40/45; conjunctive, 18/20; HD, 90/157; uncharacterized, 47/65; interneuron, 30/31; Figure 3E). Among significantly theta rhythmic cells, the depth of theta modulation varied as a function of running speed in nearly half of the cells (109 out of 235 theta-rhythmic cells; Figure S2A), indicating that these cells become more theta rhythmic at higher running speeds. This parallels previous reports that the amplitude of LFP theta oscillations increases with running speed at sites within the hippocampal formation (Hinman et al., 2011; Long et al., 2014). A majority of theta rhythmic cells also had oscillatory frequencies that significantly varied as a function of running speed (139 out of 244 theta rhythmic cells; Figure 3F), with a majority of each cell type following the same pattern (grid, 20/40; conjunctive,

13/18; HD, 50/90; uncharacterized, 26/47; interneuron, 26/30; Figure 3F). This is displayed in the plots (Figures 3A–3D) as a decrease in the lags in the peaks of the autocorrelation as a function of running speed, which, when converted to frequency, yields a positive slope between running speed and theta frequency (conversion not done for individual examples), as has been previously observed in both the LFP and single cells. Each cell type had mean positive r values and slopes between oscillatory frequency and running speed (Figures 3G and 3H), which result in approximately 0.25–0.675 Hz changes in oscillatory frequency across a typical behavioral range of running speeds (e.g., 50 cm s^{-1}). Note that this small magnitude of frequency change matches the scale required in computational models of grid cells.

As different models of grid cell firing have employed firing rate and oscillatory-frequency speed signals and both signals are present in MEC, we next asked whether the two speed signals are related to each other within individual cells. Since both the firing rate and oscillatory speed signals are positive on average, we investigated whether they are just different physiological manifestations of the same speed signal. The slope between oscillatory theta frequency and running speed is independent of each cell's slope between firing rate and running speed (Figures 3A–3D and 3I), with the correlation between the two slopes being non-significant for the entire population of speed-modulated cells (Figure 3I; r = 0.01, n.s.), as well as when each cell type was considered on its own (Figure S2H; grid, r = −0.21, n.s.; conjunctive, r = 0.41, n.s.; HD, r = 0.17, n.s.; uncharacterized, r = 0.01, n.s.; interneuron, r = −0.03, n.s.). Additionally, there was no relationship between the pseudo-r^2 values for the firing rate and oscillatory speed signals among all speed-modulated cells (Figure 3J; r = 0.15, n.s.) or for any of the cell types on their own (Figure S2I; grid, r = 0.21, n.s.; conjunctive, r = −0.31, n.s.; HD, r = 0.15, n.s.; uncharacterized, r = −0.08, n.s.; interneuron, r = 0.12, n.s.). The same pattern held when comparing the slopes and pseudo-r^2 values for the depth of theta modulation versus running speed and the firing rate versus running speed slopes and pseudo-r^2 values (Figures S2D–S2G), with all comparisons yielding non-significant correlations. Thus, the manner in which a cell's firing rate and intrinsic theta frequency vary as a function of running speed is unrelated, suggesting that firing rate and oscillatory frequency are independent cellular properties and their two respective speed signals are dissociable.

Theta Phase of Spiking

Given that the oscillatory frequency of MEC neurons increases as a function of running speed, the increase in firing rate observed in most neurons could potentially be a result of a greater number of theta cycles occurring per second with the same number of spikes within each cycle. Therefore, we investigated whether the number of spikes occurring within each theta cycle varies as a function of running speed for those cells that were identified as having significantly speed-modulated firing rates. Just as there was a mean positive relationship between firing rate and running speed, there was a mean positive slope between the number of spikes per theta cycle (SPC) and running speed for the overall set of speed-modulated neurons (Figure 4A; Wilcoxon signed-rank test, $p < 1 \times 10^{-10}$), as well as for each individual MEC cell type (Figure 4A; Wilcoxon signed-rank test; grid, $p < 1 \times 10^{-5}$; conjunctive, $p < 0.001$; HD, $p < 0.0005$; uncharacterized, $p < 0.0005$; interneuron, $p < 0.0005$). Additionally, there was a strong relationship between firing rate versus running speed slopes and the SPC versus running speed slopes (Figure 4B; all speed modulated, r = 0.84, $p < 1 \times 10^{-10}$; grid, r = 0.82, $p < 1 \times 10^{-06}$; conjunctive, r = 0.88, $p < 1 \times 10^{-05}$; HD, r = 0.79, $p < 1 \times 10^{-10}$; uncharacterized, r = 0.86, $p < 1 \times 10^{-10}$; interneuron, r = 0.71, $p < 0.0001$), and there was no relationship between the slope of SPC versus running speed and the slope of theta oscillatory frequency versus running speed (all speed modulated, r = −0.04, n.s.; grid, r = 0.26, n.s.; conjunctive, r = 0.18, n.s.; HD, r = 0.03, n.s.; uncharacterized, r = −0.27, n.s.; interneuron, r = 0.18, n.s.). This indicates that the change in firing rate as a function of running speed is not a reflection of the greater number of theta cycles per second occurring as an animal moves faster, thus further supporting the dissociation between the firing rate and oscillatory speed signals.

Neurons throughout the hippocampal formation and related structures have been shown to spike at selective phases of LFP theta rhythm (i.e., theta phase locking; Fox et al., 1986; Csicsvari et al., 1999; Mizuseki et al., 2009). The overwhelming majority of neurons were theta phase locked (257 out of 282 MEC neurons = 91%; grid, 34/38; conjunctive, 20/20; HD, 111/124; uncharacterized, 51/58; interneuron, 30/30). Since the number of spikes per theta cycle and the depth of theta modulation change as a function of running speed, we asked whether the preferred theta phase of firing and strength of theta phase locking vary as a function of running speed. Linear-circular correlations (Kempter et al., 2012) between the theta phase of spikes and running speed were computed for each theta phase-locked neuron (Figure 4C). No cells were found to have significant correlations, thus indicating that the preferred theta phase of firing does not vary as a function of running speed in MEC neurons. While the preferred theta phase of firing does not vary according to running speed, the strength of theta phase locking (mean resultant length, MRL) increases as an animal runs faster (Figure 4D). Most theta phase-locked cells had significant correlations between MRL and running speed (201 out of 257 = 78%), with all but two cells having a positive slope between MRL and running speed (Figure 4E). So despite variation in firing rate, depth of theta modulation, and oscillatory frequency as a function of running speed, MEC neurons do not show changes in preferred theta phase of firing according to running speed, but do become theta phase locked at faster running speeds.

Enhanced Firing Rate Speed Signal in the Absence of MS Input

The MS is well positioned to provide a speed signal to MEC and has been shown to be responsible for speed modulation of CA1 firing rates (Fuhrmann et al., 2015). Therefore, we tested whether the MS is responsible for propagating the speed signal present in MEC neuron firing rates by analyzing the data during pharmacological inactivation of MS during the recording of speed-modulated MEC neurons. The total proportion of MEC neurons with significantly speed-modulated firing rates did not change during

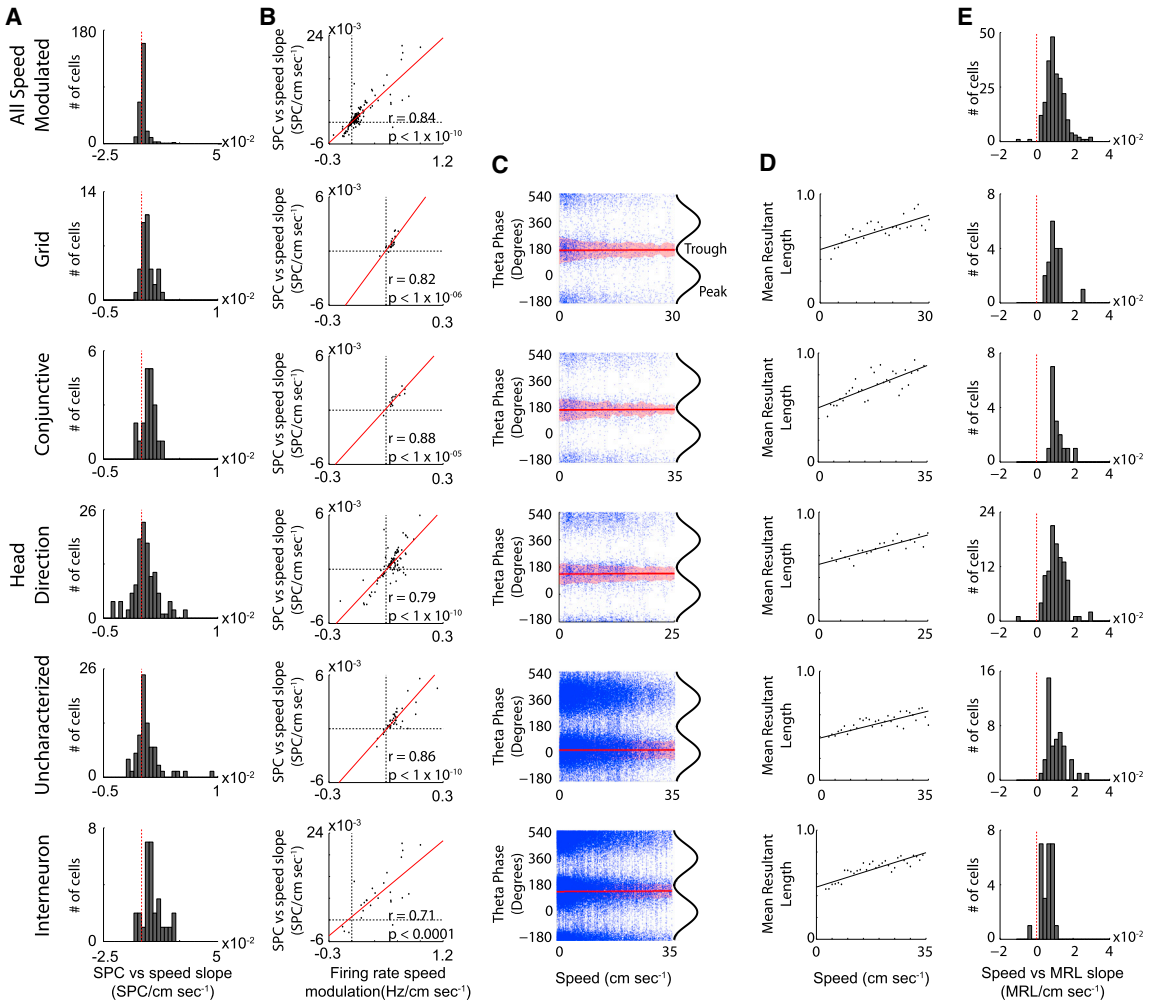

Figure 4. Increased Phase Locking as a Function of Running Speed

(A) Distributions of the slope between the number of spikes per theta cycle and running speed.

(B) Scatterplots showing the strong relationship between the SPC versus running speed slopes and the firing rate versus running speed slopes. The red line in each plot is the regression line.

(C) Theta phase of spiking versus running speed for example cells. The circular-linear best-fit line is in red and the shaded region is the circular SD of spiking at each running speed.

(D) Mean resultant length (phase locking) versus running speed for each of the cells in (C).

(E) Population distributions of slopes between mean resultant length and running speed. Virtually all cells have a positive slope between phase locking and running speed.

MS inactivation or the first recovery session (Figure 5A; MS inactivation, chi-square = 0.51, n.s.; 3–6 hr recovery, chi-square = 0.98, n.s.), nor did the proportion of linear and saturating cells (MS inactivation, chi-square = 0.04, n.s.; 3–6 hr recovery, chi-square = 0.82, n.s.), although there was a slight reduction in the proportion of speed-modulated cells during the 24 hr recovery session (chi-square = 5.75, $p < 0.05$). Given that the same proportion of cells is significantly speed modulated during MS inactivations, we next asked whether the strength of speed modulation changes. Surprisingly, speed modulation of MEC neuron firing rates became stronger during MS inactivation, as indicated by increased pseudo-r^2 values during MS inactivation as compared to baseline recordings for all MEC cells with significant speed modulation (Wilcoxon signed-rank test, $p = 1.57 \times 10^{-05}$; Figures 5B and 5C). Each cell type appeared to display a similar pattern of increased pseudo-r^2 values during MS inactivation, although subsequent statistical testing demonstrated that grid cells, uncharacterized cells, and interneurons were the only cell types to significantly increase during MS inactivation (Wilcoxon signed-rank test; grid, $p < 0.05$; conjunctive, n.s.; HD, n.s.; uncharacterized, $p < 0.005$; interneuron, $p < 0.05$; Figure 5C). The change in the pseudo-r^2 values appeared to result from a strengthening of the relationship between firing rate and running speed, as there was no significant change in the slope of the relationship (Figure S3B; Wilcoxon signed-rank test; all speed modulated, n.s.; grid, n.s.; conjunctive, n.s.; HD, n.s.;

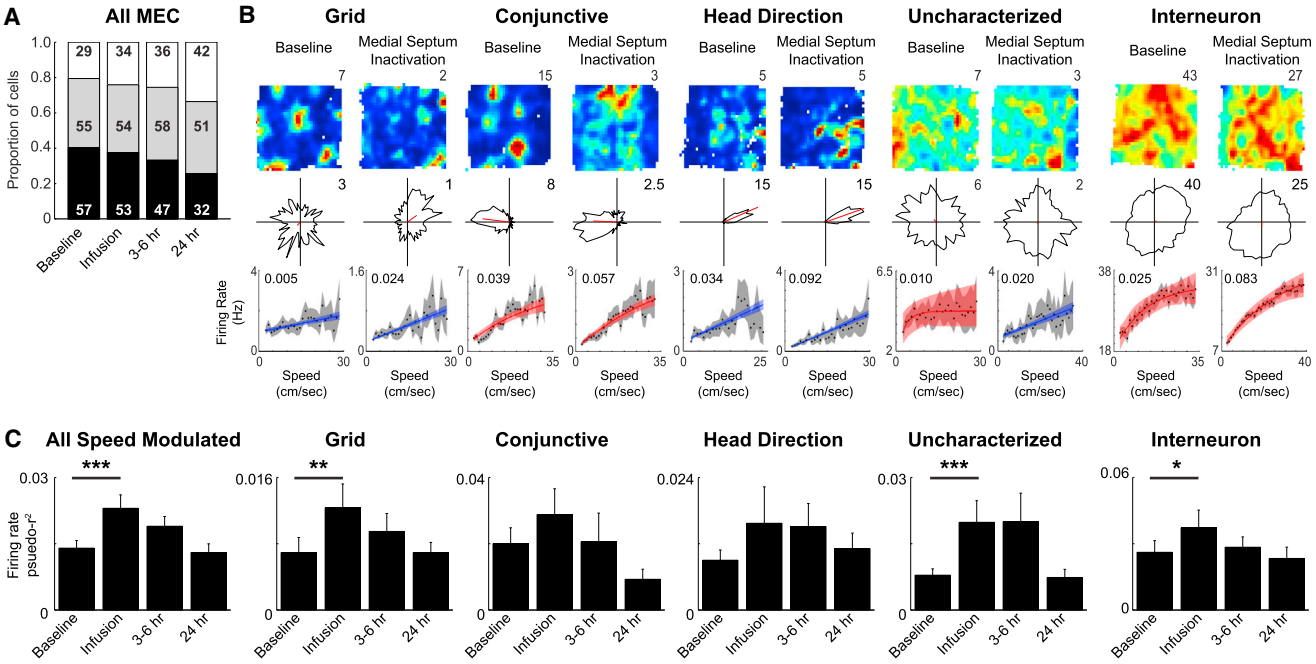

Figure 5. Enhanced Firing Rate Speed Signal during MS Inactivation

(A) Proportion of significantly speed-modulated MEC cells does not change during MS inactivation.

(B) Spatial rate maps (maximum firing rate [Hz] indicated above each map), HD polar plots (maximum radial axis limit [Hz] indicated in top right corner of each plot), and firing rate versus running speed plots with inset firing rate pseudo-r^2 values (top to bottom) during the baseline recording (left) and MS inactivation recording that commenced about 15 min after the end of the infusion (right) for an example cell.

(C) Mean ± SEM firing rate pseudo-r^2 values across each recording session showing an increase in the strength of firing rate speed modulation during MS inactivation. *$p < 0.05$, **$p < 0.005$, ***$p < 0.0005$.

uncharacterized, n.s.; interneuron, n.s.), although considering the saturating and linear separately indicated that there was a significant increase in the slopes of the linear cells and no change in the saturating cells (Wilcoxon signed-rank test; linear, $p < 0.05$; saturating, n.s.; Figure S3B). As has previously been reported (Brandon et al., 2011), the firing rate of grid cells decreased during MS inactivation, while the firing rates of the other putative principal cell types were unaffected (see Figure 3 in Brandon et al., 2011). Similarly to grid cells, interneuron firing rates also decreased during MS inactivation (Wilcoxon signed-rank test, $p < 1 \times 10^{-5}$; Figure S3A). The decrease in mean firing rate was the likely cause of a decrease observed in the y-intercept of the relationship between firing rate and running speed (Figure S3C; Wilcoxon signed-rank test; all speed modulated, $p < 8.52 \times 10^{-5}$), which was restricted to interneurons (grid, n.s.; conjunctive, n.s.; HD, n.s.; uncharacterized, n.s.; interneuron, $p < 0.0005$). In summary, in the absence of MS input, firing rates of MEC neurons become more strongly modulated by running speed.

Disrupted Oscillatory Speed Signal in the Absence of MS Input

When MS is inactivated, there is a substantial decrease in theta rhythmicity in the LFP, yet a surprising number of individual MEC cells retain theta rhythmicity in their spike trains (Brandon et al., 2011, 2013). In the cells examined during MS inactivation, there is a clear loss of theta rhythmicity in some cells, resulting in a decrease in the proportion of significantly theta rhythmic neurons during MS inactivation that return to baseline levels during recovery recordings (Figures 6A and 6B; MS inactivation, chi-square = 16.66, $p < 0.00005$; 3–6 hr recovery, chi-square = 0.17, n.s.; 24 hr recovery, chi-square = 0.01, n.s.). Despite the decrease in the proportion of theta rhythmic neurons, a majority of MEC cells actually retained theta rhythmicity during MS inactivation (73 out of 141 MEC cells; Figures 6A and 6C). Given that the firing rate speed signal remains present in MEC neurons during MS inactivation, we asked whether the cells that remain theta rhythmic during MS inactivation continue to have that oscillatory activity positively modulated by running speed. The proportion of theta rhythmic cells with speed-modulated frequencies did not significantly change during MS inactivation or either recovery session (Figure 6A; MS inactivation, chi-square = 2.21, n.s.; 3–6 hr recovery, chi-square = 0.01, n.s.; 24 hr recovery, chi-square = 0.14, n.s.), yet unlike the firing-rate speed signal that showed increased pseudo-r^2 values during MS inactivation, the pseudo-r^2 values for the oscillatory speed signal were reduced during MS inactivation among cells that remained theta rhythmic (Figure 6D; Wilcoxon signed-rank test, $p < 0.0005$), suggesting a decrement in the oscillatory speed signal in the absence of MS input. A similar pattern was observed for each individual cell type, although only the interneurons showed a statistically significant decrease during

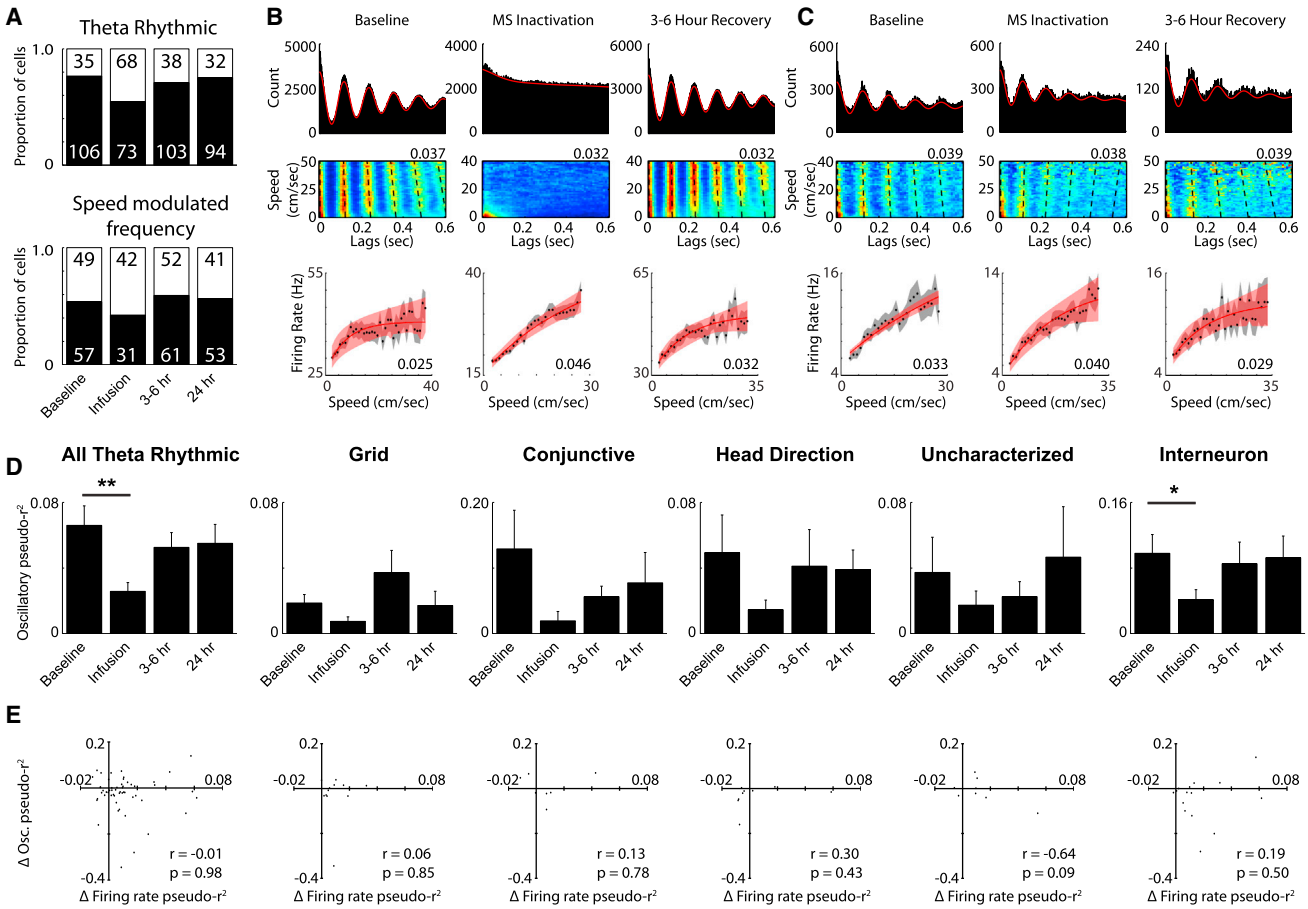

Figure 6. Disruption of Oscillatory Speed Signal during MS Inactivation

(A) The proportion of significantly theta rhythmic cells (top) and the proportion of theta rhythmic cells with significantly speed-modulated oscillatory frequencies (bottom).

(B) Traditional spike time autocorrelation (top), density plot of spike time lags as a function of running speed (the value at the top right corner of each plot indicates the maximum conditional probability of firing [red] shown in the plot and the sum of each running speed row equals a conditional probability of 1) (middle), and firing rate versus running speed plot (bottom) for an example interneuron.

(C) Same plots as in (B), but for an interneuron that remains theta rhythmic during MS inactivation.

(D) Mean ± SEM pseudo-r^2 values between oscillatory frequency and running speed for all theta rhythmic cells, and broken down by each individual cell type as well.

(E) Lack of a relationship between the change in firing rate pseudo-r^2 values and the change in oscillatory frequency pseudo-r^2 values between baseline and MS inactivation for all cell types. *$p < 0.05$, **$p < 0.0005$.

MS inactivation (Figure 6D; Wilcoxon signed-rank test, $p < 0.05$). The variation of the depth of theta modulation as a function of running speed was also decreased similarly to the modulation of frequency during MS inactivation among all theta rhythmic cells (Figure S4A; Wilcoxon signed-rank test, $p < 0.005$) and again only among the interneurons when each cell type is considered individually (Wilcoxon signed-rank test, $p < 0.05$). Overall, the strength of the coupling between oscillatory frequency and oscillatory amplitude and running speed is decreased during MS inactivation.

The slopes and r values for the firing rate and oscillatory speed signals were shown above not to be related to each other, and the two speed signals also respond in opposite directions to the removal of MS input, so we further confirmed the independence of the two signals by investigating whether any relationship exists between each cell's firing rate speed signal change and oscillatory speed signal change during MS inactivation. It is clear that the two signals are independent simply by the fact that there is a group of cells that lose theta rhythmicity, and the associated oscillatory speed signal, during MS inactivation, but have an enhanced firing rate speed signal (Figure 6B). A majority of cells that lose theta rhythmicity have either increased firing rate versus running speed pseudo-r^2 values (52%) or transition from having non-significant firing rate versus running speed relationships to significant relationships (9%) during MS inactivation (Figure S4B). Additionally, the cells that lose theta rhythmicity have significantly increased firing rate versus running speed pseudo-r^2 values during MS inactivation, similar to the overall population of speed-modulated cells (Wilcoxon signed-rank test, $p < 0.005$; Figure S4C). Yet even among cells that retain

theta rhythmicity, there is no relationship between how their oscillatory speed signal and firing speed signal changes (Figures 6C and 6E). Correlations between the change in pseudo-r^2, r value, or slope for the firing rate and oscillatory frequency speed signals were all non-significant across cell types (Figures 6E, S4F, and S4G), and the same was also true when comparing the changes to depth of theta modulation versus running speed and the firing rate speed signal changes (Figures S4D and S4E). Thus, there is not only a lack of any baseline relationship between the firing rate and oscillatory speed signals, but the two signals do not manifest related changes in response to MS inactivation.

DISCUSSION

Multiple Speed Signals in MEC

If an animal is navigating on the basis of path integration, the internal representation of its location within an environment needs to be continuously updated based on the combined information of the speed and direction of movements. Models of grid cells generally employ path-integration mechanisms in order to generate regularly repeating spatial firing fields, and these models traditionally require directional and linear speed information (McNaughton et al., 2006; Fuhs and Touretzky, 2006; Burgess et al., 2007; Hasselmo, 2008; Blair et al., 2008; Burak and Fiete, 2009). Both speed and directional information have been shown to be present in MEC (Sargolini et al., 2006; Wills et al., 2012; Brandon et al., 2013; Kropff et al., 2015). The current work detailed the multiple ways in which MEC neurons respond to running speed. First, the firing rates of the majority of MEC neurons are significantly modulated by the running speed of the animal, yet the majority of those cells had firing rates that saturate rather than linearly tracking running speed, and a sizable percentage (16%) is actually negatively modulated by running speed. Second, the majority of theta rhythmic MEC cells have an oscillatory frequency that is modulated by running speed. Third, there is no consistent relationship between the firing rate and oscillatory frequency speed signals, suggesting the two running speed signals to be independent. Fourth, inactivation of MS resulted in an increase in the strength of the relationship between firing rate and running speed, and fifth, the strength of the speed modulation of oscillatory frequency by running speed was reduced by the same MS inactivation. The results from the MS inactivation experiments provide further evidence for the independence of the two commonly employed speed signals in grid cell models and additionally help to build our understanding of the pathways by which running speed information may (or may not) reach MEC circuits.

While all path-integration-based computational models of grid cell generation require a speed signal, they differ in the physiological expression of that signal. Attractor network models generally include a firing rate-based speed signal. This type of speed signal has found support among multiple reports demonstrating the speed modulation of the firing rates of various MEC neurons (Sargolini et al., 2006; Wills et al., 2012; Kropff et al., 2015), most notably the recent report showing the existence of a dedicated group of speed cells in MEC (Kropff et al., 2015). In order to generate equally spaced and stably positioned grid firing fields, the speed signal must be linear, which is a critical aspect, as non-linearities in the speed signal will result in the accumulation of error in a path integrator. By explicitly fitting the relationship between firing rate and running speed with both a linear and non-linear function, we show that there are cells present in MEC that meet the necessity of coding running speed linearly, despite the majority of cells saturating at moderate running speeds and thus coding running speed non-linearly. This is an important facet of MEC speed coding for future studies to consider, as most of the cells identified as having a non-linear relationship between firing rate and running speed could be misidentified as having a linear relationship if only a linear fit is employed. Excluding those cells that code running speed non-linearly, there are clearly still cells that fulfill the requirement of responding linearly, and a number of those cells do not have a spatial correlate, including both putative uncharacterized principal cells and interneurons. While the current work is unable to assess the context invariance of the speed coding of these cells, as was shown for speed cells (Kropff et al., 2015), it is likely that at least some of the uncharacterized cells and interneurons with linearly responding firing rates are speed cells. In addition to identifying putative positive speed cells, we also found a sizable proportion of negatively speed-modulated cells (16%). This is an intriguing property given recent work on the presence of negatively speed-modulated cells in CA2 that code for space during immobility (Kay et al., 2016) and thus could be recipients of input from negatively speed-modulated MEC cells via entorhinal-hippocampal synapses (Chevaleyre and Siegelbaum, 2010) or alternatively could provide negatively speed-modulated output back to MEC via hippocampal-entorhinal projections (Rowland et al., 2013).

Unlike attractor dynamic models of grid cells, oscillatory interference models generally employ a speed signal present in the oscillatory frequency of cell spiking rhythmicity. The oscillatory theta frequency of cells has previously been shown to increase as a function of running speed in MEC (Jeewajee et al., 2008; Brandon et al., 2013), hippocampus (Geisler et al., 2007; Welday et al., 2011), MS (King et al., 1998; Welday et al., 2011),and anterior thalamus (Welday et al., 2011), as well as the frequency of LFP theta oscillations throughout the hippocampal formation (Rivas et al., 1996; Sławińska and Kasicki, 1998; Jeewajee et al., 2008; Hinman et al., 2011). The current findings further support the speed-dependent variation of oscillatory theta frequency of single-cell spiking through the use of a novel maximum likelihood estimation approach to identifying variation in rhythmic properties as a function of running speed. This technique allows for the examination of continuous behavioral segments and is more robust in detecting significant rhythmicity with lower spike counts than previously employed approaches (Climer et al., 2015). A majority of the theta rhythmic MEC cells had oscillatory frequencies that significantly varied according to running speed, which included cells of every subtype considered (Figure 3), and the slope of the relationship matched that typically employed by oscillatory interference models. Virtually all interneurons had speed-modulated oscillatory frequencies, which lends support to recent grid

cell modeling work that employed theta rhythmic inhibition from MEC interneurons to grid cells that has a speed-modulated frequency as a mechanism for coding running speed (Hasselmo and Shay, 2014).

Given that both the firing rate and oscillatory frequency of MEC neurons generally showed increases as a function of running speed, we addressed the question as to whether perhaps the speed-dependent firing rate and oscillatory frequency changes within a single cell were related physiological manifestations of a single running speed signal impinging upon MEC circuits. This was not the case, as there was no correlation between the manner in which a cell's firing rate and oscillatory frequency varied as a function of running speed. The independence of the two signals was further supported by the opposite direction of the changes in the strength of each signal during MS inactivation, with the firing rate speed signal becoming stronger and the oscillatory frequency speed signal becoming weaker across the overall population. Two critical questions are raised by the effects of MS inactivation on the two speed signals. First, what is the function of each speed signal given that they are simultaneously present within the same circuit, and can we identify whether one or the other is necessary for the generation of grid cells? It is difficult to conceptualize a system in which both speed signals operate simultaneously within the same circuit for the same purpose, whether that is generating grid cells or not. Second, given that neither speed signal was abolished during MS inactivations, by what anatomical pathway does running speed information reach MEC? Below, we discuss each of these questions, with the latter addressed first, followed by the former.

Locomotion-modulated firing rates have been observed in an overwhelmingly large number of cortical and subcortical structures (outside of motor generation regions), including primary visual cortex (Niell and Stryker, 2010), primary auditory cortex (Fu et al., 2014), barrel cortex (Fu et al., 2014), retrosplenial cortex (Cho and Sharp, 2001), posterior parietal cortex (Whitlock et al., 2012), postrhinal cortex (Furtak et al., 2012), entorhinal cortex (Sargolini et al., 2006; Wills et al., 2012; Kropff et al., 2015), striatum (Yeshenko et al., 2004), medial and lateral septum (King et al., 1998; Zhou et al., 1999), lateral hypothalamus (Bender et al., 2015), and the hippocampus (McNaughton et al., 1983). It is difficult to identify any single circuitry that could propagate running speed information throughout the hippocampal formation based on these varied structures, but recently glutamatergic neurons in MS were shown to be responsible for speed modulation in CA1 (Fuhrmann et al., 2015). Yet despite the fact that MS projects strongly to MEC (Kondo and Zaborszky, 2016) and our inactivations abolished LFP theta oscillations and grid cells in MEC (Brandon et al., 2011), speed modulation of MEC firing rates was actually enhanced during MS inactivations in opposition to our hypothesis. The possibility exists that running speed signals emanate from a more ventral region in the diagonal band of Broca that our inactivation may not have reached. One possible mechanism for the enhancement of the firing rate speed signal in MEC during MS inactivation is that the speed signal emanating from the hippocampus is lost, as is suggested by recent work demonstrating that MS glutamatergic neurons are responsible for speed modulation in hippocampus. Given that speed cells in MEC and hippocampus show prospective and retrospective relationships with running speed, respectively (Kropff et al., 2015), the removal of the slightly temporally misaligned hippocampal speed signal input to MEC may lead to the observed enhanced firing rate speed signal in MEC.

As for the first question raised by the presence of two independent running speed signals in MEC, it seems unlikely that both signals could provide running speed information used to update a path integrator. In principle, modeling work demonstrates the feasibility of either signal providing running speed information, but there is currently no indication that both signals could be used simultaneously. One possibility is that the different speed signals arise from different sources, with one speed signal coding the self-motion signal from the brainstem whereas another speed signal may arise from computation of speed based on changes in visual stimuli such as optic flow (Raudies and Hasselmo, 2015). Given that most models of grid cells are based on path integration, requiring both direction and running speed information, manipulation of either component should result in corresponding changes in grid cell firing. Removal of HD information results in the loss of grid cells (Winter et al., 2015), although it is not known whether the same manipulation also alters the coding of running speed. During MS inactivation, HD cells remain intact (Brandon et al., 2011), yet grid cell spatial periodicity is disrupted (Brandon et al., 2011; Koenig et al., 2011). The current work demonstrated that during MS inactivation, when grid cells are disrupted there are alterations of both the firing rate coding of running speed and the rhythmicity code for running speed that could lead to changes in path integration in different grid cell models. A path integrator using a firing rate speed signal, as in attractor dynamic models, that is enhanced during MS inactivation would result in a change in grid cell spatial scale, which is not observed during MS inactivation. Alternatively, a path integrator using a rhythmicity speed signal coded by changes in frequency, as in oscillatory interference models, would accumulate error with the diminished coding of speed by frequency of rhythmicity observed during MS inactivation.

Another possibility is that one of the speed signals maintains an alternative purpose. The running speed of an animal has profound effects on temporal coordination throughout the hippocampal formation. Movement through space is one of the most basic behaviors performed by an animal, and as the rate of movement through space increases, most other behaviors of the animal must be performed with increasing speed. Perceptual judgments, memory-based decisions, and motor outputs must all take place on shorter timescales with less temporal allowance for correcting erroneous neuronal computations or behavioral actions. Such a situation requires faster and/or more efficient intra- and inter-regional communication, which can be achieved through increased phase locking, faster frequency oscillations, and greater coherence between sites.

Activity throughout MEC and much of the hippocampal formation becomes increasingly tuned within the theta frequency range at faster running speeds. Theta coherence between MEC and the hippocampus, as well as across the

septotemporal axis of the hippocampus, increases as a function of running speed (Hinman et al., 2011, 2013), thus potentially satisfying the need for more efficient intra- and inter-regional communication. The increase in theta frequency both intrinsically within individual cells and in the LFP translates to shorter cycle durations and thus to information transfer at shorter timescales. The current work demonstrated that in addition to oscillating at a faster frequency, the magnitude of the intrinsic rhythmicity of MEC neurons is also increased as an animal runs faster. The increased depth of theta rhythmic firing by MEC neurons likely contributes to the increase in LFP theta amplitude observed as an animal runs faster (McFarland et al., 1975; Kemere et al., 2013) and will increasingly bring their postsynaptic targets into the theta rhythmic regime.

Neurons in MEC not only exhibit increased theta rhythmicity as a function of running speed, but we have also shown that they become increasingly theta phase locked at faster running speeds. Theta phase locking of spikes increased, while the theta phase at which they spike does not vary. Maintaining the same theta phase of firing across different running speeds maintains constant phase relationships between different cell populations, such as the two groups of entorhinal neurons that fire on opposite phases of theta (Mizuseki et al., 2009; Newman and Hasselmo, 2014). Overall, this tuning in the theta frequency range at faster running speeds may allow for more efficient communication on shorter timescales throughout the entorhino-hippocampal memory circuit during behaviors that restrict the time allowed for processing incoming information and executing memory-based actions.

EXPERIMENTAL PROCEDURES

Subjects

This paper uses data gathered during experiments for which some results have previously been published (Brandon et al., 2011, 2013). Six adult male Long-Evans rats (500–650 g) obtained from Charles River Labs were used. All experimental procedures were approved by the Institutional Animal Care and Use Committee for the Charles River Campus at Boston University. Detailed methods are provided in the Supplemental Experimental Procedures.

Statistics

Normality of distributions was not assumed, so comparisons were made using non-parametric statistics. Comparisons of single distributions for a difference from zero were performed using Wilcoxon signed-rank tests. For comparisons of two distributions, Wilcoxon signed-rank or Wilcoxon rank-sum tests were used. The general approach taken was to perform the various statistical tests on the full set of relevant cells and then divide the cells into the different functional cell types and perform the same statistical test on each individual cell type.

SUPPLEMENTAL INFORMATION

Supplemental Information includes Supplemental Experimental Procedures and four figures and can be found with this article online at http://dx.doi.org/10.1016/j.neuron.2016.06.027.

AUTHOR CONTRIBUTIONS

M.P.B. and M.E.H. designed the experiments. M.P.B. conducted experiments. J.R.H., J.R.C., and G.W.C. analyzed data. J.R.H., J.R.C., G.W.C., and M.E.H. wrote the paper.

ACKNOWLEDGMENTS

Support for this work was provided by ONR MURI grant N00014-10-1-0936, NIMH R01 MH60013, and MH61492.

Received: April 22, 2015
Revised: March 1, 2016
Accepted: June 10, 2016
Published: July 14, 2016

REFERENCES

Alonso, A., and Köhler, C. (1984). A study of the reciprocal connections between the septum and the entorhinal area using anterograde and retrograde axonal transport methods in the rat brain. J. Comp. Neurol. *225*, 327–343.

Bender, F., Gorbati, M., Cadavieco, M.C., Denisova, N., Gao, X., Holman, C., Korotkova, T., and Ponomarenko, A. (2015). Theta oscillations regulate the speed of locomotion via a hippocampus to lateral septum pathway. Nat. Commun. *6*, 8521.

Blair, H.T., Gupta, K., and Zhang, K. (2008). Conversion of a phase- to a rate-coded position signal by a three-stage model of theta cells, grid cells, and place cells. Hippocampus *18*, 1239–1255.

Brandon, M.P., Bogaard, A.R., Libby, C.P., Connerney, M.A., Gupta, K., and Hasselmo, M.E. (2011). Reduction of theta rhythm dissociates grid cell spatial periodicity from directional tuning. Science *332*, 595–599.

Brandon, M.P., Bogaard, A.R., Schultheiss, N.W., and Hasselmo, M.E. (2013). Segregation of cortical head direction cell assemblies on alternating θ cycles. Nat. Neurosci. *16*, 739–748.

Buetfering, C., Allen, K., and Monyer, H. (2014). Parvalbumin interneurons provide grid cell-driven recurrent inhibition in the medial entorhinal cortex. Nat. Neurosci. *17*, 710–718.

Burak, Y., and Fiete, I.R. (2009). Accurate path integration in continuous attractor network models of grid cells. PLoS Comput. Biol. *5*, e1000291.

Burgess, N. (2008). Grid cells and theta as oscillatory interference: theory and predictions. Hippocampus *18*, 1157–1174.

Burgess, N., Barry, C., and O'Keefe, J. (2007). An oscillatory interference model of grid cell firing. Hippocampus *17*, 801–812.

Bush, D., and Burgess, N. (2014). A hybrid oscillatory interference/continuous attractor network model of grid cell firing. J. Neurosci. *34*, 5065–5079.

Buzsáki, G. (2002). Theta oscillations in the hippocampus. Neuron *33*, 325–340.

Chevaleyre, V., and Siegelbaum, S.A. (2010). Strong CA2 pyramidal neuron synapses define a powerful disynaptic cortico-hippocampal loop. Neuron *66*, 560–572.

Cho, J., and Sharp, P.E. (2001). Head direction, place, and movement correlates for cells in the rat retrosplenial cortex. Behav. Neurosci. *115*, 3–25.

Climer, J.R., DiTullio, R., Newman, E.L., Hasselmo, M.E., and Eden, U.T. (2015). Examination of rhythmicity of extracellularly recorded neurons in the entorhinal cortex. Hippocampus *25*, 460–473.

Csicsvari, J., Hirase, H., Czurkó, A., Mamiya, A., and Buzsáki, G. (1999). Oscillatory coupling of hippocampal pyramidal cells and interneurons in the behaving Rat. J. Neurosci. *19*, 274–287.

Czurkó, A., Huxter, J., Li, Y., Hangya, B., and Muller, R.U. (2011). Theta phase classification of interneurons in the hippocampal formation of freely moving rats. J. Neurosci. *31*, 2938–2947.

Fox, S.E., Wolfson, S., and Ranck, J.B., Jr. (1986). Hippocampal theta rhythm and the firing of neurons in walking and urethane anesthetized rats. Exp. Brain Res. *62*, 495–508.

Fu, Y., Tucciarone, J.M., Espinosa, J.S., Sheng, N., Darcy, D.P., Nicoll, R.A., Huang, Z.J., and Stryker, M.P. (2014). A cortical circuit for gain control by behavioral state. Cell *156*, 1139–1152.

Fuhrmann, F., Justus, D., Sosulina, L., Kaneko, H., Beutel, T., Friedrichs, D., Schoch, S., Schwarz, M.K., Fuhrmann, M., and Remy, S. (2015).

Locomotion, theta oscillations, and the speed-correlated firing of hippocampal neurons are controlled by a medial septal glutamatergic circuit. Neuron *86*, 1253–1264.

Fuhs, M.C., and Touretzky, D.S. (2006). A spin glass model of path integration in rat medial entorhinal cortex. J. Neurosci. *26*, 4266–4276.

Furtak, S.C., Ahmed, O.J., and Burwell, R.D. (2012). Single neuron activity and theta modulation in postrhinal cortex during visual object discrimination. Neuron *76*, 976–988.

Fyhn, M., Molden, S., Witter, M.P., Moser, E.I., and Moser, M.B. (2004). Spatial representation in the entorhinal cortex. Science *305*, 1258–1264.

Geisler, C., Robbe, D., Zugaro, M., Sirota, A., and Buzsáki, G. (2007). Hippocampal place cell assemblies are speed-controlled oscillators. Proc. Natl. Acad. Sci. USA *104*, 8149–8154.

Guanella, A., and Verschure, P.F. (2006). A model of grid cells based on path integration mechanism. In Artificial Neural Networks–ICANN 2006, S.D. Kollias, A. Stafylopatis, W. Duch, and E. Oja, eds. (Springer), pp. 740–749.

Hafting, T., Fyhn, M., Molden, S., Moser, M.B., and Moser, E.I. (2005). Microstructure of a spatial map in the entorhinal cortex. Nature *436*, 801–806.

Hasselmo, M.E. (2008). Grid cell mechanisms and function: contributions of entorhinal persistent spiking and phase resetting. Hippocampus *18*, 1213–1229.

Hasselmo, M.E. (2013). Neuronal rebound spiking, resonance frequency and theta cycle skipping may contribute to grid cell firing in medial entorhinal cortex. Philos. Trans. R. Soc. Lond. B Biol. Sci. *369*, 20120523.

Hasselmo, M.E., and Brandon, M.P. (2012). A model combining oscillations and attractor dynamics for generation of grid cell firing. Front. Neural Circuits *6*, 30.

Hasselmo, M.E., and Shay, C.F. (2014). Grid cell firing patterns may arise from feedback interaction between intrinsic rebound spiking and transverse traveling waves with multiple heading angles. Front. Syst. Neurosci. *8*, 201.

Hinman, J.R., Penley, S.C., Long, L.L., Escabí, M.A., and Chrobak, J.J. (2011). Septotemporal variation in dynamics of theta: speed and habituation. J. Neurophysiol. *105*, 2675–2686.

Hinman, J.R., Penley, S.C., Escabí, M.A., and Chrobak, J.J. (2013). Ketamine disrupts theta synchrony across the septotemporal axis of the CA1 region of hippocampus. J. Neurophysiol. *109*, 570–579.

Jeewajee, A., Barry, C., O'Keefe, J., and Burgess, N. (2008). Grid cells and theta as oscillatory interference: electrophysiological data from freely moving rats. Hippocampus *18*, 1175–1185.

Kay, K., Sosa, M., Chung, J.E., Karlsson, M.P., Larkin, M.C., and Frank, L.M. (2016). A hippocampal network for spatial coding during immobility and sleep. Nature *531*, 185–190.

Kemere, C., Carr, M.F., Karlsson, M.P., and Frank, L.M. (2013). Rapid and continuous modulation of hippocampal network state during exploration of new places. PLoS ONE *8*, e73114.

Kempter, R., Leibold, C., Buzsáki, G., Diba, K., and Schmidt, R. (2012). Quantifying circular-linear associations: hippocampal phase precession. J. Neurosci. Methods *207*, 113–124.

King, C., Recce, M., and O'Keefe, J. (1998). The rhythmicity of cells of the medial septum/diagonal band of Broca in the awake freely moving rat: relationships with behaviour and hippocampal theta. Eur. J. Neurosci. *10*, 464–477.

Koenig, J., Linder, A.N., Leutgeb, J.K., and Leutgeb, S. (2011). The spatial periodicity of grid cells is not sustained during reduced theta oscillations. Science *332*, 592–595.

Kondo, H., and Zaborszky, L. (2016). Topographic organization of the basal forebrain projections to the perirhinal, postrhinal, and entorhinal cortex in rats. J. Comp. Neurol. *524*, 2503–2515, http://dx.doi.org/10.1002/cne.23967.

Kropff, E., Carmichael, J.E., Moser, M.B., and Moser, E.I. (2015). Speed cells in the medial entorhinal cortex. Nature *523*, 419–424.

Long, L.L., Hinman, J.R., Chen, C.M., Escabi, M.A., and Chrobak, J.J. (2014). Theta dynamics in rat: speed and acceleration across the Septotemporal axis. PLoS ONE *9*, e97987.

Maurer, A.P., Vanrhoads, S.R., Sutherland, G.R., Lipa, P., and McNaughton, B.L. (2005). Self-motion and the origin of differential spatial scaling along the septo-temporal axis of the hippocampus. Hippocampus *15*, 841–852.

McFarland, W.L., Teitelbaum, H., and Hedges, E.K. (1975). Relationship between hippocampal theta activity and running speed in the rat. J. Comp. Physiol. Psychol. *88*, 324–328.

McNaughton, B.L., Barnes, C.A., and O'Keefe, J. (1983). The contributions of position, direction, and velocity to single unit activity in the hippocampus of freely-moving rats. Exp. Brain Res. *52*, 41–49.

McNaughton, B.L., Battaglia, F.P., Jensen, O., Moser, E.I., and Moser, M.B. (2006). Path integration and the neural basis of the 'cognitive map'. Nat. Rev. Neurosci. *7*, 663–678.

Mitchell, S.J., Rawlins, J.N., Steward, O., and Olton, D.S. (1982). Medial septal area lesions disrupt theta rhythm and cholinergic staining in medial entorhinal cortex and produce impaired radial arm maze behavior in rats. J. Neurosci. *2*, 292–302.

Mizumori, S.J., Perez, G.M., Alvarado, M.C., Barnes, C.A., and McNaughton, B.L. (1990). Reversible inactivation of the medial septum differentially affects two forms of learning in rats. Brain Res. *528*, 12–20.

Mizuseki, K., Sirota, A., Pastalkova, E., and Buzsáki, G. (2009). Theta oscillations provide temporal windows for local circuit computation in the entorhinal-hippocampal loop. Neuron *64*, 267–280.

Navratilova, Z., Giocomo, L.M., Fellous, J.M., Hasselmo, M.E., and McNaughton, B.L. (2012). Phase precession and variable spatial scaling in a periodic attractor map model of medial entorhinal grid cells with realistic after-spike dynamics. Hippocampus *22*, 772–789.

Newman, E.L., and Hasselmo, M.E. (2014). Grid cell firing properties vary as a function of theta phase locking preferences in the rat medial entorhinal cortex. Front. Syst. Neurosci. *8*, 193.

Niell, C.M., and Stryker, M.P. (2010). Modulation of visual responses by behavioral state in mouse visual cortex. Neuron *65*, 472–479.

Raudies, F., and Hasselmo, M.E. (2015). Differences in visual-spatial input may underlie different compression properties of firing fields for grid cell modules in medial entorhinal cortex. PLoS Comput. Biol. *11*, e1004596.

Rivas, J., Gaztelu, J.M., and García-Austt, E. (1996). Changes in hippocampal cell discharge patterns and theta rhythm spectral properties as a function of walking velocity in the guinea pig. Exp. Brain Res. *108*, 113–118.

Rowland, D.C., Weible, A.P., Wickersham, I.R., Wu, H., Mayford, M., Witter, M.P., and Kentros, C.G. (2013). Transgenically targeted rabies virus demonstrates a major monosynaptic projection from hippocampal area CA2 to medial entorhinal layer II neurons. J. Neurosci. *33*, 14889–14898.

Sargolini, F., Fyhn, M., Hafting, T., McNaughton, B.L., Witter, M.P., Moser, M.B., and Moser, E.I. (2006). Conjunctive representation of position, direction, and velocity in entorhinal cortex. Science *312*, 758–762.

Schmidt-Hieber, C., and Häusser, M. (2013). Cellular mechanisms of spatial navigation in the medial entorhinal cortex. Nat. Neurosci. *16*, 325–331.

Sławińska, U., and Kasicki, S. (1998). The frequency of rat's hippocampal theta rhythm is related to the speed of locomotion. Brain Res. *796*, 327–331.

Stensola, H., Stensola, T., Solstad, T., Frøland, K., Moser, M.B., and Moser, E.I. (2012). The entorhinal grid map is discretized. Nature *492*, 72–78.

Taube, J.S. (2007). The head direction signal: origins and sensory-motor integration. Annu. Rev. Neurosci. *30*, 181–207.

Vanderwolf, C.H. (1969). Hippocampal electrical activity and voluntary movement in the rat. Electroencephalogr. Clin. Neurophysiol. *26*, 407–418.

Welday, A.C., Shlifer, I.G., Bloom, M.L., Zhang, K., and Blair, H.T. (2011). Cosine directional tuning of theta cell burst frequencies: evidence for spatial coding by oscillatory interference. J. Neurosci. *31*, 16157–16176.

Whitlock, J.R., Pfuhl, G., Dagslott, N., Moser, M.B., and Moser, E.I. (2012). Functional split between parietal and entorhinal cortices in the rat. Neuron *73*, 789–802.

Wills, T.J., Barry, C., and Cacucci, F. (2012). The abrupt development of adult-like grid cell firing in the medial entorhinal cortex. Front. Neural Circuits *6*, 21.

Winson, J. (1978). Loss of hippocampal theta rhythm results in spatial memory deficit in the rat. Science *201*, 160–163.

Winter, S.S., Clark, B.J., and Taube, J.S. (2015). Spatial navigation. Disruption of the head direction cell network impairs the parahippocampal grid cell signal. Science *347*, 870–874.

Yeshenko, O., Guazzelli, A., and Mizumori, S.J. (2004). Context-dependent reorganization of spatial and movement representations by simultaneously recorded hippocampal and striatal neurons during performance of allocentric and egocentric tasks. Behav. Neurosci. *118*, 751–769.

Zhou, T.L., Tamura, R., Kuriwaki, J., and Ono, T. (1999). Comparison of medial and lateral septal neuron activity during performance of spatial tasks in rats. Hippocampus *9*, 220–234.

Zilli, E.A. (2012). Models of grid cell spatial firing published 2005-2011. Front. Neural Circuits *6*, 16.

Neuron, Volume *91*

Supplemental Information

Multiple Running Speed Signals in Medial Entorhinal Cortex

James R. Hinman, Mark P. Brandon, Jason R. Climer, G. William Chapman, and Michael E. Hasselmo

Supplemental Figure 1

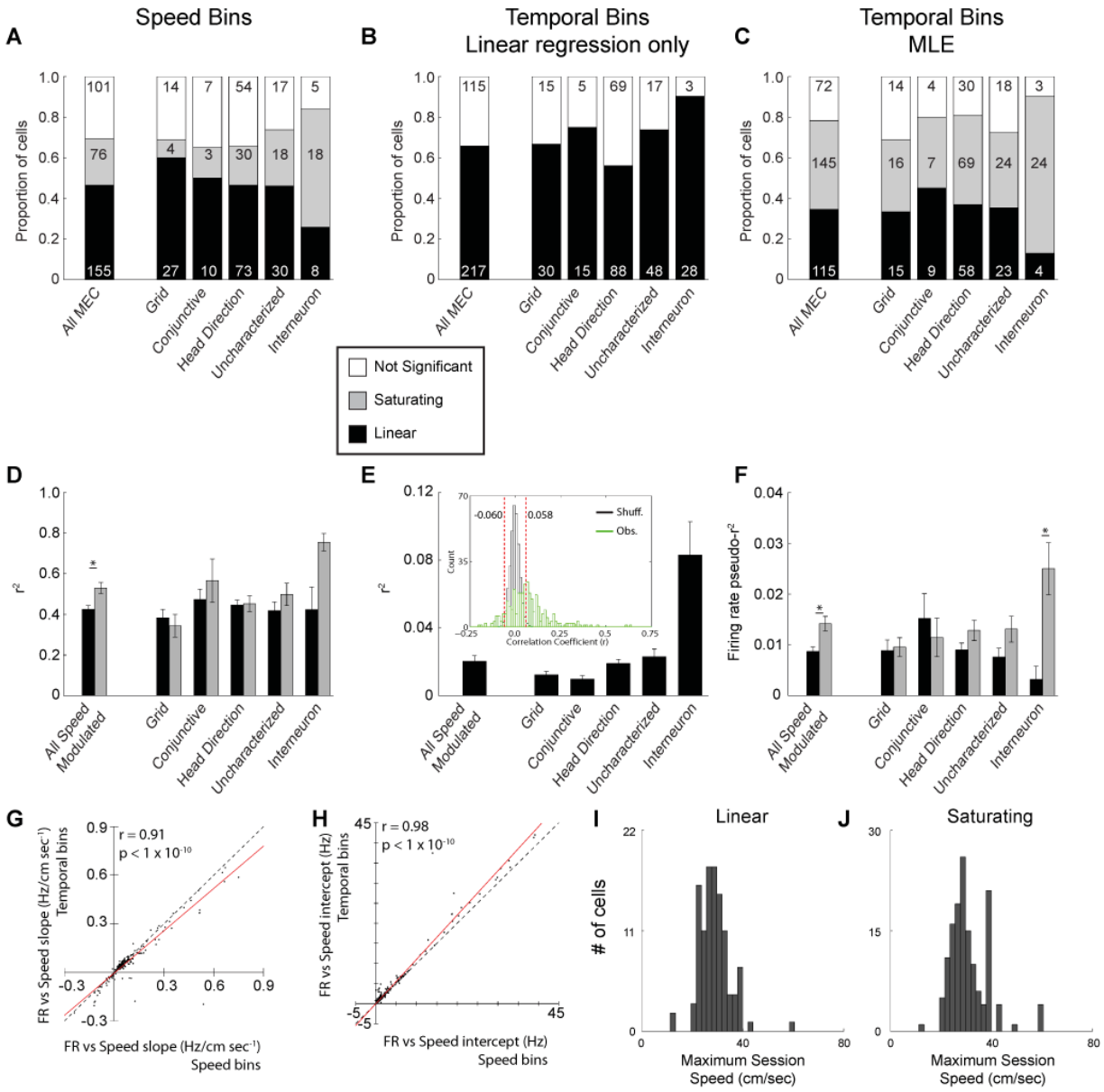

Figure S1. Related to Figure 1. Comparison of multiple approaches of identifying speed modulation. A) Binning data according to speed yields qualitatively similar proportions of speed modulated cells, although there is a tendency to overestimate the number of linearly speed coding cells. B) Performing a linear regression on temporally binned data and using a shuffling procedure to set a significance threshold identifies a qualitatively similar proportion of speed modulated cells, but by definition cannot identify non-linear firing rate to running speed relationships. C) Same plot as in Figure 1C shown again for comparative purposes. D) Mean +/- SEM r^2 values for the significantly speed modulated cells identified using the speed binned data. Note that this approach over estimates the amount of variance explained by running speed. E) Mean +/- SEM r2 values for the significantly speed modulated cells identified using temporal bins, linear regression and thresholds obtained through a shuffling procedure. The inset plot shows the distribution of shuffled correlation coefficients (black) with the counts normalized by the number of shuffles (100x per cell) and the distribution of observed correlation coefficients (green). Dashed red lines show the 1st and 99th percentile thresholds of the shuffled distribution. F) Same plot as in

Figure 1D shown again for comparative purposes. G) Scatter plot showing the similarity of the firing rate versus running speed slopes obtained using speed binned and temporally binned data. Red line shows regression line. H) Same as in G, but for the y-intercept. I) Distribution of maximum session running speed for cells identified as linear. J) Same as in *I*, but for cells identified as saturating.

Supplemental Figure 2

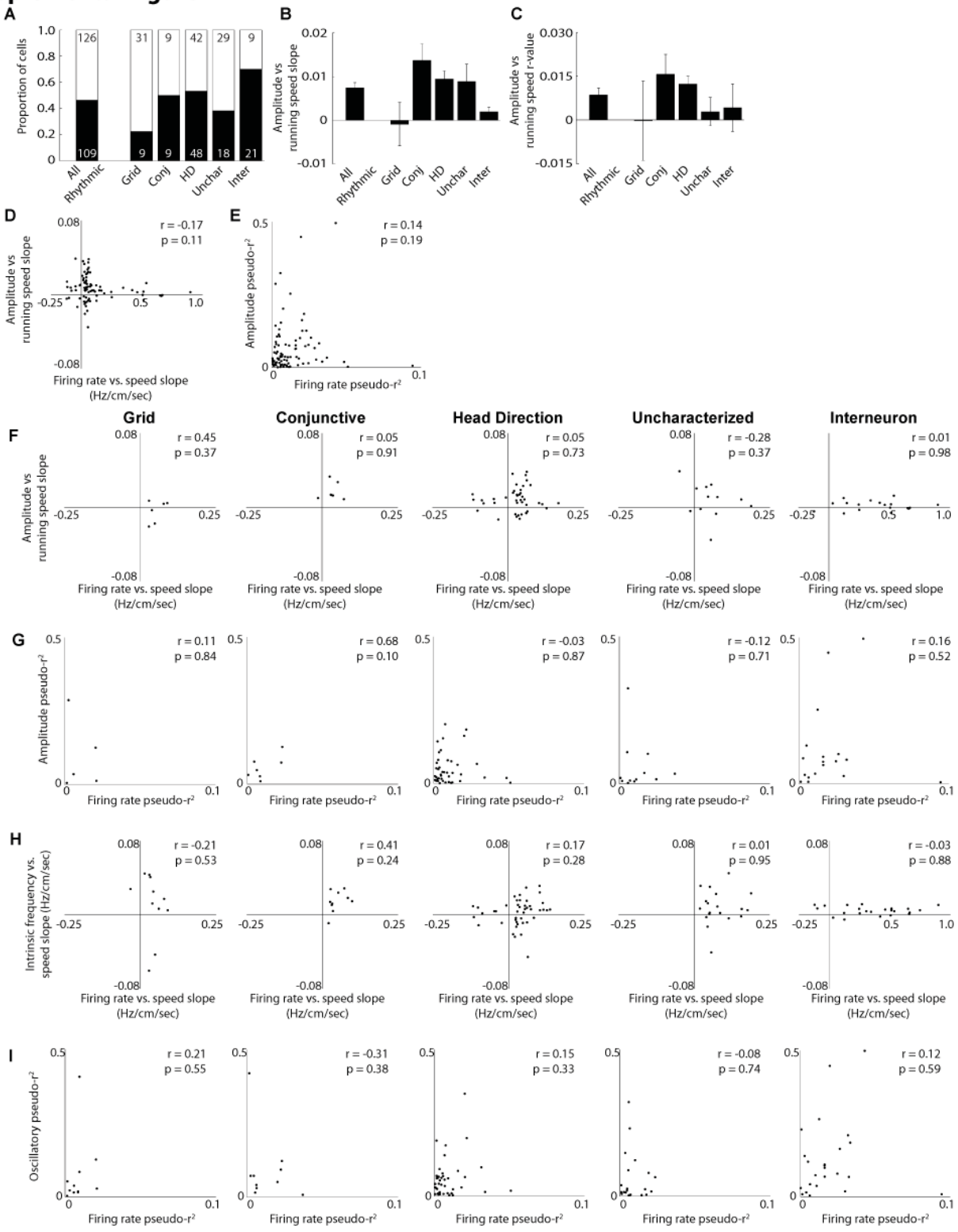

Figure S2. Related to Figure 3. A) Proportion of theta rhythmic cells with significant variation in the depth of theta modulation as a function of running speed. B) Mean +/- SEM slope of the relationship between the depth of theta modulation versus running speed. C) Mean +/- SEM r-value of the relationship between the depth of theta

modulation versus running speed. D) Scatterplot showing the lack of a relationship between slopes for firing rate versus running speed and depth of theta modulation versus running speed. E) Same as in D, but for the r-values. F) Data as in D broken down by cell type. G) Data as in E broken down by cell type. H) Data as in Figure 3I broken down by cell type. I) Data as in Figure 3J broken down by cell type.

Supplemental Figure 3

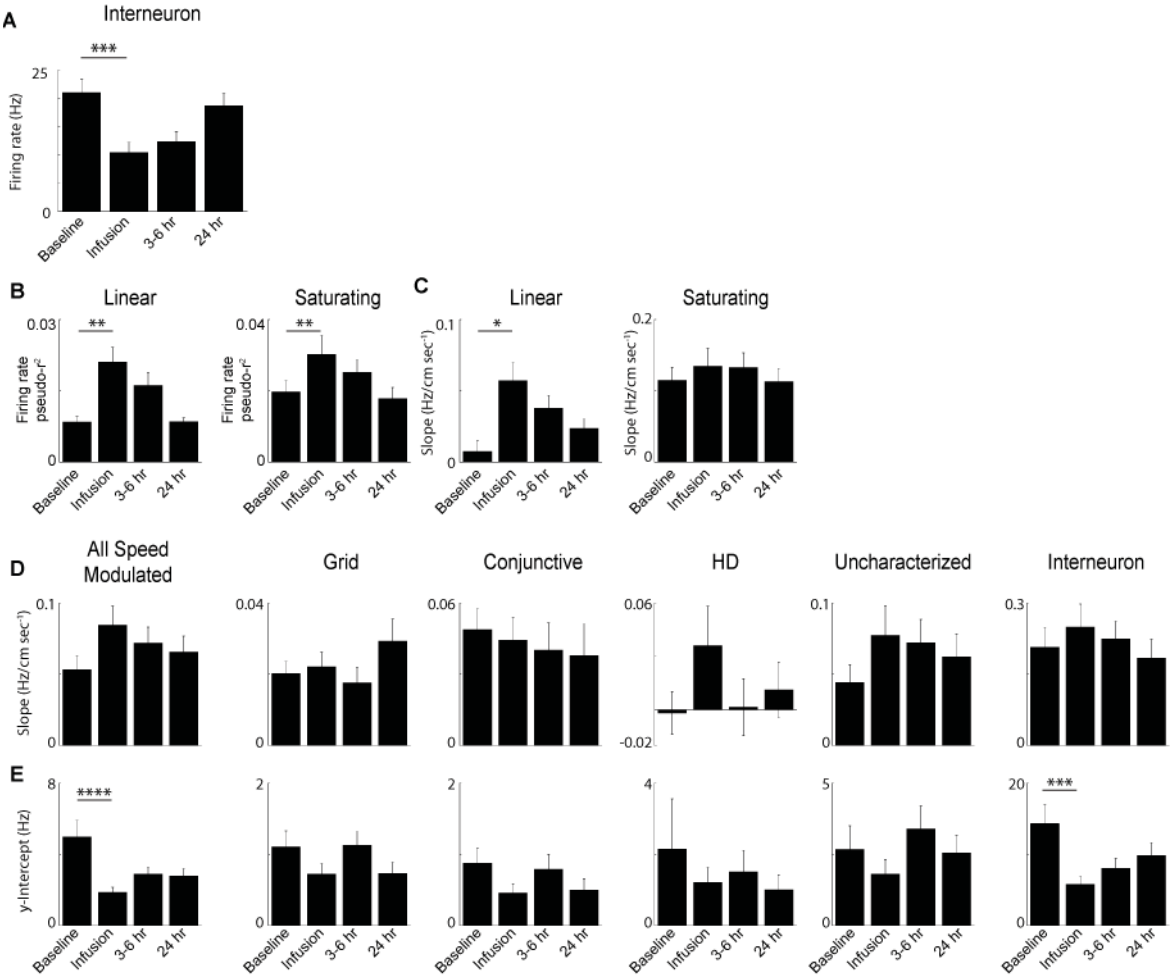

Figure S3. Related to Figure 5. A) Interneuron firing rates across Baseline, MS infusion and two recovery sessions. B) Firing rate versus running speed pseudo-r^2 values for Linear and Saturating cells during Baseline, MS infusion and two recovery sessions. C) Firing rate versus running speed slope values for Linear and Saturating cells during Baseline, MS infusion and two recovery sessions. D) Firing rate versus running speed slopes during Baseline, MS infusion and two recovery sessions. E) Same as B but for y-intercepts. * $p < 0.05$, ** $p < 0.01$, *** $p < 0.0005$, **** $p < 0.00005$

Supplemental Figure 4

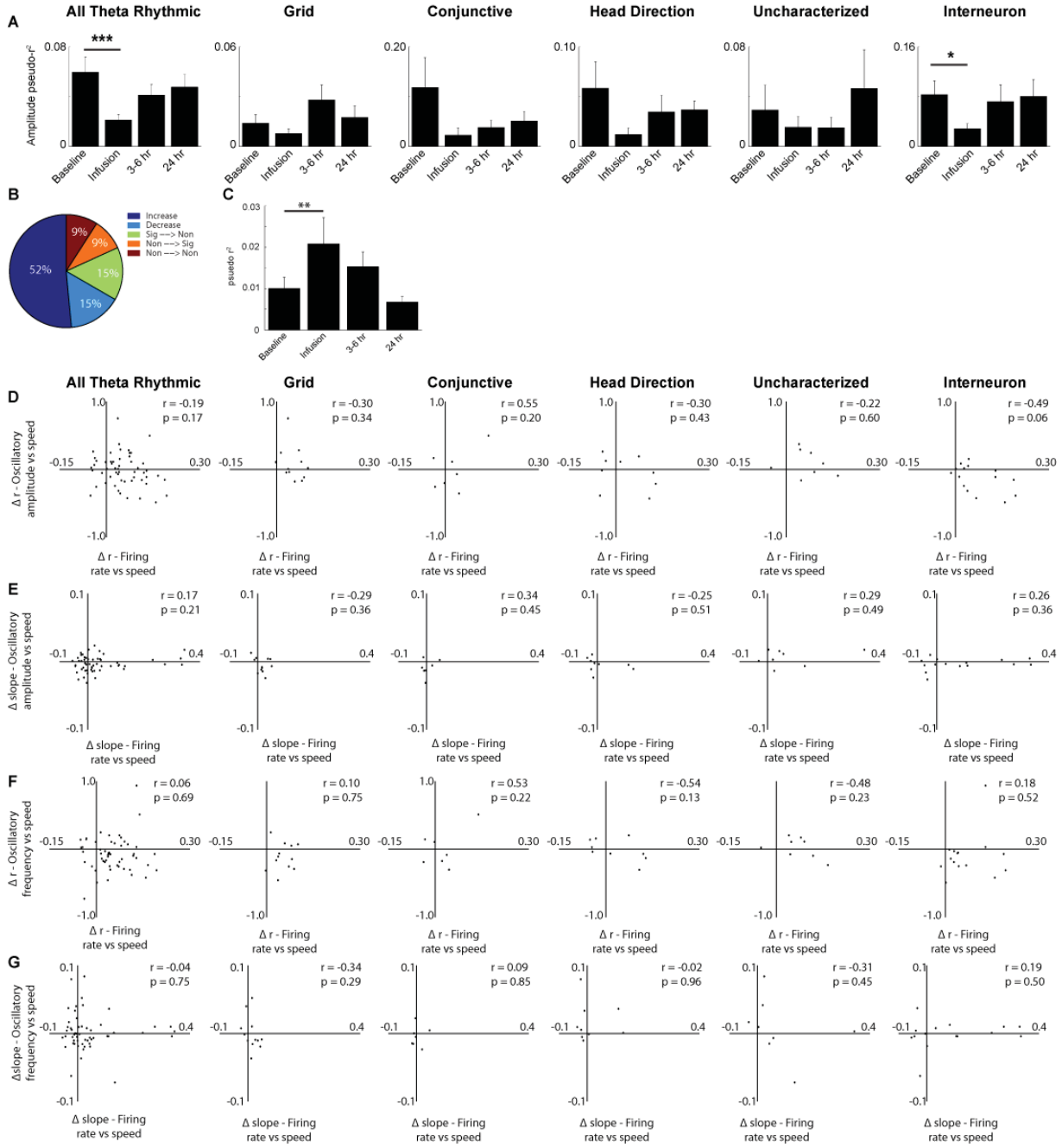

Figure S4 Related to Figure 6. A) Mean +/- SEM pseudo-r^2 of the relationship between depth of theta modulation and running speed for Baseline, MS infusion, 3-6 hour and 24 hour recovery sessions. B) Proportion of cells showing various changes in the strength of firing rate speed modulation among those cells that lost theta rhythmicity during MS infusion. C) Mean firing rate versus running speed pseudo-r^2 of the cells that lost theta rhythmicity during MS infusion. D) Scatterplots showing the lack of a relationship between the change in the r-values for firing rate versus running speed and depth of theta modulation versus running speed. E) Same as in D, but for the change in slope. F) Scatterplots showing the lack of a relationship between the change in r-values for firing rate versus running speed and oscillatory frequency versus running speed. G) Same as in F, but for the change in slope. * $p < 0.05$, ** $p < 0.005$, *** $p < 0.0005$

Supplemental Experimental Procedures

Subjects: This paper uses data gathered during experiments for which some results have previously been published (Brandon et al., 2011, 2013). Six adult male Long-Evans rats (500-650g) obtained from Charles River Labs (Wilmington, MA) were used. All animals were cared for using standard procedures that included individually housing them in plexiglass cages and maintaining them on a 12/12 hour light/dark cycle in a temperature and humidity controlled facility. All experimental procedures were approved by the Institutional Animal Care and Use Committee for the Charles River Campus at Boston University.

Presurgical Procedures: Prior to surgery animals were habituated to both the testing environment and being handled by experimenters. All animals were maintained at ~85% of their *ad libitum* weight in order to facilitate foraging for small pieces of Froot Loops (General Mills, Battle Creek, MI) in an open field environment (100 by 115 cm or 112 by 158 cm). Both open field environments contained a large white cue card on one wall and animals were familiarized with foraging for cereal pieces in the open field, as well as having contact with the experimenter.

Surgery: The surgical procedures have previously been described in detail (Brandon et al., 2011, 2013), but, briefly, a custom built hyperdrive housing 12 tetrodes aimed at dorsomedial entorhinal cortex and one or two infusion cannula directed at the medial septum were implanted. Atropine (0.04 mg/kg) was administered prior to induction of anesthesia. All surgical procedures were conducted under anesthesia induced with Isoflurane and a ketamine cocktail (Ketamine: 12.92 mg/kg, Acepromazine: 0.1 mg/kg, Xylazine: 1.31 mg/kg). Upon the loss of toe pinch reflex rats were placed in a stereotaxic frame, a midline incision was made in the skin above the skull and the skull was cleared of all connective tissue. Anchor screws were positioned across the skull surrounding the implant sites for the MS cannula (AP: +0.5 mm, ML: 2.0 mm, DV: 4.5 mm relative to bregma and penetrating the brain at a 20° angle) and the MEC hyperdrive (AP: -6.0 mm, ML: 4.5 mm relative to bregma). After lowering the cannula into the brain it was secured to the anchor screws with dental cement. Upon lowering the hyperdrive to the surface of the brain the remaining space in the skull hole was filled with silicone and then the hyperdrive was secured to the anchor screws with dental cement. A ground screw was positioned over the cerebellum. Once all of the implants were firmly secured in position, tetrodes were lowered 2 – 3 mm from the dorsal surface of the brain. After surgery animals were allowed to recover for seven days prior to any experimental involvement.

Behavioral testing and medial septal inactivation: All recordings were obtained while rats foraged for small pieces of Froot Loops in a large open field environment (100 by 115 cm or 112 by 158 cm) that had a large white cue card on one wall. Each recording session lasted 20 minutes. A subset of recording sessions involved pharmacological inactivations of MS with the $GABA_A$ agonist muscimol. A pre-infusion baseline recording session was conducted prior to any infusions that lasted 20 minutes. The protocol for muscimol infusions has been described previously (Brandon et al., 2011, 2013). The injector cannula was primed and inserted into the guide cannula where it extended 1mm beyond the end of the guide cannula. A total volume of 0.5 µL of muscimol diluted in phosphate-buffered saline was infused with a microinfusion pump (Harvard Aparatus, Holliston, MA) at a rate of 0.125 µL/min. At the

end of the four minute injection the infusion cannula was left in place for an additional two minutes to allow proper diffusion of the solution away from the injection site. After waiting 15 minutes from the end of the infusion, a post-infusion recording was begun that lasted up to 60 minutes. A recovery recording was conducted 3-6 hours after the infusion and an additional recovery session was attempted 24 hours after the infusion when cells could be stably held across days with each recording lasting 20 minutes.

Electrophysiological data acquisition: Electrophysiological recordings were obtained as rats foraged in an open field environment. All neural signals were pre-amplified on the headstage and subsequently transmitted to a Digital Lynx SX data acquisition system (Neuralynx, Bozeman, MT) where the signals were amplified (5,000 – 20,000X) and bandpass filtered (0.3-6 kHz.). Spikes were detected online as a threshold crossing on any of the four wires of a tetrode, at which point a window around the threshold crossing was digitized at 32 kHz and stored for later analysis. Position and head direction information of the rat was obtained via an overhead video camera that monitored two LEDs attached to the headstage.

Cell classification: The various functional cell types found in MEC were identified using established approaches. Ratemaps were generated by aligning spike time stamps to behavioral data such that each spike fell within a single frame of behavioral data. The firing rate within each spatial bin was calculated as the number of spikes occurring while the animal was in that spatial bin over the total amount of time spent within the bin. These normalized 2D histograms were smoothed by a two-dimensional 3cm Gaussian Kernel to generate the final ratemap. Gridness scores were calculated as published previously (Brandon et al., 2011). This method takes the two-dimensional autocorrelation of the rate map and draws a ring to encompass the six peaks nearest to the center of the autocorrelogram. The inner radius of this ring is defined as one half the minimum distance from the center of the autocorrelation to adjacent peaks. The outer radius was allowed to vary from the same size as the inner radius to the edge of the autocorrelation map. Gridness scores for each ring is defined as the difference between the lowest correlation of a rotation observed at 60 or 120 degrees of rotation and the highest correlation observed at 30, 90 or 150 degrees. The final gridness score for the cell session is then calculated as the maximum gridness score among all of the rings.

Consistent with previous approaches, HD cells were identified based on the Watson's U^2 score of their head directional tuning curves (Johnson et al., 2005). The Watsons's U^2 statistic was chosen over other scores (such as mean-resultant length) because it is non-parametric, requiring no binning of data points and making no assumptions that the tuning curve is unimodal.

Border cells show a higher firing rate along one or more boundaries of the environment, thus a border score was employed as in (Solstad et al., 2008). This border score is defined as:

$$\frac{Cm - Dm}{Cm + Dm}$$

Where Dm is the normalized mean distance from the location of a spike to the nearest wall and Cm is the proportion of pixels along a wall greater than 60% of the max spatial firing rate. While border cells were identified amongst

the recorded cells, the number was generally low and therefore summary data for border cells is not presented as is done for the other cell types.

Using the spatial firing property scores described above, each cell was assigned to a single functional cell type. Grid cells were identified as those cells with a gridness score greater than 0.34 and Watson's U^2 value less than 8, while conjunctive grid-by-head direction cells were those cells with a gridness score greater than 0.34 and a Watson's U^2 greater than 8. Head direction cells were classified as those cells having a Watson's U^2 score greater than or equal to 8, but not showing the spatial periodicity of grid cells. Border cells were defined based on a border score of 0.5 or greater while also not having any single field over 1/3 the size of the entire environment (Solstad et al., 2008), but very few cells met this criterion and thus they were not considered further. Putative interneurons were identified as those cells that did not meet any functional cell class criteria, had mean firing rates greater than 8 Hz and waveforms with peak-to-trough durations less than 0.275 ms in line with previously published reports (Buetfering et al., 2014; Mizuseki et al., 2009). Cells that did not meet any functional cell class criteria or the firing rate and waveform shape criteria for interneurons were designated as 'uncharacterized' cells.

Temporally binned firing rate versus running speed and MLE: Firing rate was fit using a maximum likelihood estimator. The instantaneous running speed was taken from the Kalman velocity, based on displacement in location between each recorded tracking sample (Fyhn et al, 2004). The number of spikes x occurring in each video frame (30Hz) was counted. Only frames with instantaneous velocity greater than 2 cm sec^{-1} and less than the 95th percentile of running speeds were considered, in order to avoid under sampled regions. The firing rate parameter (λ) was assumed to follow one of two functions of running speed:

Linear:

$$\hat{\lambda} = \hat{b} \cdot v + \hat{a}$$

Saturating exponential:

$$\hat{\lambda} = \hat{k} - \hat{m} \cdot e^{-\hat{q} \cdot v}$$

Using a Poisson link function, the underlying firing rate parameter was fit using the 'mle' function within the MATLAB statistics toolbox. The log-likelihood for each of these generating functions was calculated and used to determine the F-value and p-score of each fit compared to the uniform fit, as well as a nested comparison of the saturating exponential to linear functions. A shuffling procedure was used in order to generate a distribution of p-values resulting from fitting spikes that are decoupled from the behavior of the animal. Spikes were shuffled by adding an independent random delay to each spike time. Random delays were taken from a uniform distribution ranging from 30 seconds to the duration of the session minus 30 seconds. If the shuffled spike time was past the end of the session, then it was wrapped around to the beginning of the session. The result is an essentially random spike series that is decoupled both from the behavior of the animal and any temporal structure between spikes. For each shuffle the random data was fit with both the linear and saturating exponential functions as described above. This was repeated 100 times for each cell and a distribution of the p-values from all cells was generated separately for both fits. The 1st percentile of both distributions was identified, which fell at p = 0.005 for the linear fit and p =

0.0065 for the saturating exponential fit. A significance threshold was then conservatively set at a p-value of 0.001 for each F-test, thus ensuring that cells identified as being significantly speed modulated met a p-value threshold smaller than that of more than 99% of the shuffled distributions. Under the null hypothesis for the nested model, the F statistic should be distributed on $F_{3-2,n-3}$ where n is the number of frames observed.

Because the relative number of spikes counted in each frame is relatively variable due to their stochastic nature, we used a pseudo-R^2 as a goodness of fit measure. Pseudo-R^2 values were calculated by estimating the portion of the variance or residual sum of squares in the counts of spikes in each frame explained by the model not explained by a Poisson variability, or

Pseudo-$R^2 = \frac{RSS_{ModelExplained}}{RSS_{Total} - RSS_{Poisson}} = \frac{\left(Var(x) - \frac{1}{n}\sum_{i=1}^{n}\left(x_i - \hat{\lambda}\right)^2\right)}{Var(x) - \bar{x}}$

$Var(x)$ is the sample variance, $\hat{\lambda}$ is the instantaneous rate predicted by the fit, x_i is the i^{th} observed count of spikes in a single frame, and n is the number of observations. Thus, $Var(x) - \frac{1}{n}\sum_{i=1}^{n}\left(x_i - \hat{\lambda}\right)^2$ is the variance remaining after accounting for the fit. For a series of independent Poisson observations, the variance is the average rate. For n large, this can be approximated by the average count in each frame, or $\bar{x}$. Thus, $Var(x) - \bar{x}$ is the variance unexplained by a simple Poisson process.

Velocity binned firing rate versus running speed: The instantaneous running speed was taken as the Kalman velocity based on displacement in location between each recorded tracking sample (Fyhn et al, 2004). Running speed was sorted into 1 cm/s bins and only speed bins that had at least 3 seconds of data over the course of the behavioral session were included in further analysis, thus resulting in each session having slightly different maximum running speeds for this analysis. The firing rate as a function of running speed for each cell was calculated as the number of spikes in each 1 cm/s bin of running speed divided by the total time spent in that speed bin. Confidence intervals for each speed bin were determined by the inverse pdf of the assumed underlying poisson. The firing rate of each cell as a function of running speed was fit with both a linear and saturating exponential function as above.

Temporally binned firing rate versus running speed and linear regression: The instantaneous firing rate was taken as the number of spikes in a videoframe, divided by the duration of the videoframe (0.33 seconds), and smoothed with a Gaussian filter with \sigma of 33ms and width of 330ms. This smoothed instantaneous firing rate was linearly correlated with the instantaneous velocity to give a Pearson-Correlation coefficient ([-1 1]). To determine critical values of this coefficient we shuffled each cell's spike times 100 times. Spikes were shuffled by adding an independent random delay to each spike time. Random delays were taken from a uniform distribution ranging from 30 seconds to the duration of the session minus the duration of the session. If the shuffled spike time was past the end of the session, then it was wrapped to the beginning of the session. The result is an essentially random spike series which is decoupled both from the behavior of the animal and any temporal structure between spikes. Cells were identified as speed modulated if the correlation coefficient was below the 1st percentile or greater than the 99th percentile of this shuffled distribution.

Rhythmic properties and covariation with speed: The properties of rhythmicity were examined using a variation of the maximum likelihood estimation approach (Climer et al., 2015), and the code is available at https://github.com/jrclimer/mle_rhythmicity. Briefly, a list of lags x_i was generated by finding all of the times a spike was found in a 2 second window following a spike, and subtracting the difference. A probability density function for these bins was defined as:

$$\mathcal{L}(x;\tau,b,c,f,s,r) = D\left((1-b)\exp\left(-\frac{x}{10^{\tau}}\right)\left(r\exp\left(-\frac{x}{10^{c}}\right)F(x) + 1\right)\right)\frac{\left(\left(2+2\sqrt{1-s}-s\right)\cos(2\pi f x)+4\,s\cos(\pi f x)+2-2\sqrt{1-s}-3s\right)}{4}$$

$$\frac{\left(\left(2+2\sqrt{1-s}-s\right)\cos(2\pi f x)+4\,s\cos(\pi f x)+2-2\sqrt{1-s}-3s\right)}{4}$$

Where $\mathcal{L}$ is the probability of a lag at time x, 10^{τ} is an overall exponential falloff rate caused by the animal leaving the high firing states of the neuron, b is a baseline, 10^{c} is an exponential falloff to the rhythmicity caused by variation in the frequency, f is the mean frequency of the modulation, s is the amount of theta cycle skipping between 0 and 1, r is the rhythmicity factor and D is a normalization factor such that $\int_{x=0}^{2}\mathcal{L}(x;\tau,b,c,f,s,r)=1$. The exponential falloff parameters τ and c measure the slow falloff in the number of spikes and the amplitude of the rhythm in autocorrelograms. For a more intuitive sense of these parameters, we encourage the reader to explore Dynamic Figure 1 from Climer et al 2015, available at http://bit.ly/1tJurco. We fit the data to this distribution by finding the maximum log likelihood, first by approximating the values using a particle swarm optimizer (Chen, 2014) and then using the *mle* function in MATLAB (MathWorks Natick, MA). To conditionalize the amplitude or frequency of the rhythmicity in the running speed of the animal, we first shifted the velocity to have zero mean. We then modeled τ, f and r as linearly varying with the running speed of the animal. We first estimated the full fit of the data using the *mle* function, first by holding the other values constant at the initial fit, and the other parameters with a zero slope and y-intercept from the initial fit. This gave estimated slopes and intercepts for τ, f and r. We then estimated the full fit using MLE from this point, giving intercepts (log10(sec), Hz, and unitless for τ, f and r) and slopes ($\frac{\log_{10} sec}{\frac{cm}{sec}}, \frac{Hz}{\frac{cm}{sec}}$, and $\frac{1}{\frac{cm}{sec}}$ respecitlvey). Significance was determided by comparing the maximum log likelihood to the maximum log likelihood when the parameters f or r were held constant. The slopes and y-intercept for the depth of modulation, a, were determined by scaling the terms for r by $(1-b)$. To plot the rhythmicity over the velocity, spikes were binned using 0.02 second time bins and 50 speed bins spanning 0 to the 99th percentile of speeds, occupancy normalized, and smoothed by a Gaussian kernel with a standard deviation of 1 bin.

We measured the goodness of the speed-modulated fits by the deviance of the speed modulated fit and the baseline rhythmic fit from a uniform fit, or:

Pseudo $R^2 = 1 - \frac{LL_{unif} - LL_A}{LL_{unif} - LL_0}$

Where $LL_{unif}, LL_A, and\ LL_0$ are the log-likelihoods of the uniform, speed-modulated, and baseline rhythmic fits respectively. This differs from the speed modulation of firing rates because we are comparing to the baseline rhythmic fit, rather than an overall constant rate. To determine the significance of these rhythmic fits we used a partial F test, comparing the log-likelihood of a uniform, non-speed modulated rhythmic, and speed modulated rhythmic distributions. The deviance between any two models was taken as twice the difference in the log-likelihood and compared to a chi squared distribution.

Theta phase locking: Local field potential theta signals were obtained by filtering the raw LFP data with a third order band pass Butterworth filter with a high pass value of 6 Hz and a low pass value of 10 Hz. The instantaneous theta phase and magnitude were calculated as the angle and magnitude of the Hilbert transform of the filtered theta signal, respectively. The preferred theta phase of firing and strength of theta phase locking of the spiking of each cell was calculated using the mean resultant angle (MRA) and length (MRL) respectively and were calculated as follows:

$$mra = atan2\big(imag(mean(e^{j\theta})), real(mean(e^{j\theta}))\big)$$

$$mrl = abs\big(mean(e^{j\theta})\big)$$

Where j is the imaginary constant, θ is the theta phase of each spike, atan2 is the four-quadrant arc tangent function, and imag() and real() represent the real and imaginary components of the complex exponential. Intuitively, this is equivalent to taking the mean of the sine and cosine separately. In order to ensure that changes in phase locking occurring as a function of speed were not the result of a different number of spikes occurring at different speeds a subsampling procedure was implemented. All subsampling was performed by finding the speed bin with the lowest number of spikes and permuting all other speed bins to have the same total number of spikes. Note that spikes in each bin were permuted, so that each spike could only be chosen once.

Linear-circular correlations: Linear-circular correlations (speed vs preferred phase) were performed as in previous reports (Kempter et al., 2012). Circular-linear slopes were found using the *fminsearch* function of MATLAB to minimize the error of:

$$R = \sqrt[2]{\left(\frac{1}{n}\sum_{i=1}^{n}\cos(\theta_i - sx_i)\right)^2 + \left(\frac{1}{n}\sum_{i=1}^{n}\sin(\theta_i - sx_i)\right)^2}$$

Where x is a sample of the linear variable, theta is a sample of the circular variable, s is the circular-linear slope and *i* is an index into the *n* samples of the variable. *fminsearch* finds the value of s which minimizes R.

Spikes per cycle and definition of cycle bounds: The Hilbert transform used in the rest of the methods places the beginning of a theta cycle (0°) at the peak of theta. However, for a subset of analyses (change in preferred phase as a function of running speed) we calculated the mean resultant angle of theta phase of spiking and subtracted half of

this from the phase of theta. After rewrapping the resulting phase vector to [0 2*pi] the result is that for all cells the preferred angle of spiking relative to this shifted theta phase is pi.

Statistics: Normality of distributions was not assumed, so comparisons were made using non-parametric statistics. Comparisons of single distributions for a difference from zero were performed using Wilcoxon sign-rank tests. For comparisons of two distributions Wilcoxon sign-rank or Wilcoxon rank-sum tests were used. The general approach taken was to perform the various statistical tests on the full set of relevant cells and then divide the cells into the different functional cell types and perform the same statistical test on each individual cell type.

Supplemental References

Brandon MP, Bogaard AR, Libby CP, Connerney MA, Gupta K, Hasselmo ME (2011) Reduction of theta rhythm dissociates grid cell spatial periodicity from directional tuning. *Science* 332(6029): 595-599.

Brandon MP, Bogaard AR, Schultheiss NW, Hasselmo ME (2013) Segregation of cortical head direction cell assemblies on alternating theta cycles. *Nat Neurosci* 16(6): 739-48.

Buetfering C, Allen K, Monyer H (2014) Parvalbumin interneurons provide grid cell-driven recurrent inhibition in the medial entorhinal cortex. *Nat Neurosci* 17(5): 710 – 718.

Chen SS. 2014. Another particle swarm toolbox. (http://www.mathworks.com/matlabcentral/fileexchange/25986), MATLAB Central File Exchange. Retrieved August 7, 2014.

Climer JR, Ditullio R, Newman EL, Hasselmo ME, Eden UT (2015) Examination of rhythmicity of extracellularly recorded neurons in the entorhinal cortex. *Hippocampus* 25(4): 460-473.Fyhn M, Molden S, Witter MP, Moser EI, Moser MB (2004) Spatial representation in the entorhinal cortex. *Science* 305(5688): 1258-1264.

Johnson A, Seeland K, Redish AD (2005) Reconstruction of the postsubiculum head direction signal from neural ensembles. *Hippocampus* 15(1): 86-96.

Kempter R, Leibold C, Buzsaki G, Diba K, Schmidt R (2012) Quantifying circular-linear associations: hippocampal phase precession. *J Neurosci Methods* 207(1): 113 – 124.

Mizuseki K, Sirota A, Pastalkova E, Buzsaki G (2009) Theta oscillations provide temporal windows for local circuit computation in the entorhinal-hippocampal loop. *Neuron* 64(2): 267-280.

Solstad T, Boccara CN, Kropff E, Moser MB, Moser EI (2008) Representation of geometric borders in the entorhinal cortex. *Science* 322(5909): 1865-1868.